INTERNATIONAL JOURNAL FOR NUMERICAL METHODS IN FLUIDS, VOL. 26, 403–442 (1998)

VISCOUS OSCILLATORY FLOW AROUND A CIRCULAR CYLINDER AT LOW KEULEGAN–CARPENTER NUMBERS AND FREQUENCY PARAMETERS

G. ILIADIS AND P. ANAGNOSTOPOULOS*

Division of Hydraulics and Environmental Engineering, Department of Civil Engineering, Aristotle University of Thessaloniki, Thessaloniki 54006, Greece

SUMMARY

The results of a numerical study of the viscous oscillating flow around a circular cylinder at low Keulegan–Carpenter numbers (KC) and frequency parameters (β) are presented in this paper. The finite element method was used for the solution of the Navier–Stokes equations in the formulation where the streamfunction and vorticity are the field variables. The computation was conducted at Keulegan–Carpenter numbers extending up to $KC = 15$ and frequency parameters ranging between $\beta = 6$ and 100. At low values of the Keulegan–Carpenter number the flow remains symmetrical. As the Keulegan–Carpenter number is increased over a certain value which depends also on the frequency parameter, asymmetries appear in the flow which are eventually amplified and lead finally to complex vortex-shedding patterns, some of which are markedly different from those observed at higher frequency parameters. The solution revealed that although for certain values of KC and β the shedding of vortices is periodic, there also exists a complicated flow regime in which the flow is not periodic but switches between different modes in consecutive cycles of flow oscillation. For the various flow cases examined, the traces of the hydrodynamic forces are presented and the hydrodynamic coefficients and RMS values of the in-line force are compared with experimental evidence. © 1998 John Wiley & Sons, Ltd.

Int. J. Numer. Meth. Fluids, **26**: 403–442 (1998).

KEY WORDS: oscillating flow; Keulegan–Carpenter number; finite element method; in-line force; transverse force

1. INTRODUCTION

Oscillatory flow past a circular cylinder is a flow phenomenon which has proved to be a challenging area for research, since it provides a simplified tool for the investigation of flow around a cylinder immersed in a wave environment. The phenomenon is controlled by two dimensionless numbers, the Keulegan–Carpenter number (KC) and the Reynolds number (Re). KC is defined as

$$KC = U_m T/D, \tag{1}$$

Correspondence to: P. Anagnostopoulos, Division of Hydraulics and Environmental Engineering, Department of Civil Engineering, Aristotle University of Thessaloniki, Thessaloniki 54006, Greece. Contract grant sponsor: Science Programame of the European Community; Contract grant number: SC1*-CT92-0812
Contract grant sponsor: Greek Foundation of National Awards (IKY).

CCC 0271–2091/98/040403–40 $17.50

Received April 1996
Revised April 1997

where U_m is the maximum flow velocity, T is the period of oscillation and D is the cylinder diameter. The Reynolds number is

$$Re = U_m D/v, \tag{2}$$

where v is the kinematic viscosity. The ratio of these two numbers is known as the frequency parameter (β) and is defined as

$$\beta = Re/KC = D^2/vT. \tag{3}$$

Several experimental investigations of the phenomenon have been conducted throughout a wide range of Reynolds and Keulegan–Carpenter numbers. Experiments at low KC have revealed that the flow can be classified into a number of different flow regimes governed mainly by KC and dependent also on Re.[1–3] At $KC \ll 1$ the flow remains attached, symmetrical and two-dimensional. As KC increases, the flow separates from the cylinder and remains symmetrical, until KC reaches a critical threshold whose value depends on the frequency parameter. If this critical KC is exceeded, the flow becomes asymmetric and various vortex-shedding flow regimes are observed in which the number of vortices shed in each oscillation cycle increases with the Keulegan–Carpenter number. Although several investigators have proposed ranges of KC for particular types of vortex shedding, more than one shedding mode is possible even when KC and β are fixed, as reported by Bearman *et al.*,[1] and the flow may switch between different modes. Bearman *et al.*[1] described the transverse vortex-shedding regime in the interval $8 < KC < 15$ and the diagonal shedding mode in the interval $15 < KC < 25$. Williamson[2] observed the transverse street ($7 < KC < 13$), single-pair ($13 < KC < 15$), double-pair ($15 < KC < 24$) and triple-pair ($24 < KC < 32$) regimes with increasing KC. The diagonal shedding of Bearman *et al.*[1] is an alternative definition of the double pair described by Williamson,[2] since in both studies two vortex pairs are convected away from the cylinder in opposite directions during one cycle. Tatsuno and Bearman[4] conducted a flow visualization study for a large number of KC and β pairs, where KC extended up to 15 and β was lower than 160. Their investigation revealed eight flow regimes within this KC and β range and the great significance of β in the form of the flow pattern for constant KC. It is interesting to note that some of the regimes detected by Tatsuno and Bearman[4] do not seem to occur at higher values of β. Honji[5] conducted a flow visualization study of oscillatory flow which revealed that a three-dimensional instability develops at small KC. This three-dimensional instability was further studied by Sarpkaya[3] and Tatsuno and Bearman.[4]

Attached oscillatory flow at very small KC was studied analytically by Stokes.[6] Wang[7] obtained a solution of the Navier–Stokes equations valid for $KC \ll 1$ and $\beta \gg 1$ and proposed formulae for the drag and inertia coefficients. For values of β higher than 1000, Sarpkaya[3] found differences between his measured drag values and those predicted by Wang's[7] analysis for $KC > 0{\cdot}7$, and attributed the discrepancy to the three-dimensional instability quoted before.

With the increasing efficiency of digital computers, the numerical solution of the phenomenon in two dimensions became feasible. Baba and Miyata[8] presented a finite difference solution for $KC = 5$ and 7 and $Re \approx 1000$. The flow pattern in this simulation was symmetrical, therefore physically unrealistic. Murashige *et al.*[9] used a similar technique to analyse the flow at $KC = 5$, 7 and 10 for Re extending up to 10,000. The flow was perturbed artificially for the generation of asymmetry, therefore agreement with the physical phenomenon was obtained. Wang and Dalton[10] obtained a finite difference solution of the Navier–Stokes equations for $KC = 1$–12 and $Re = 100$–3000. Justesen[11] conducted a detailed computational study of planar oscillatory flow, also employing the finite difference technique, for β ranging between 196 and 1035 and KC extending up to 26. He observed various vortex-shedding regimes when KC exceeded approximately 7, while his computed drag values were very similar to those predicted by Wang[7] for KC extending up to 1·5 for $\beta = 1035$ and up to 2 for lower values of β. This constitutes very strong support for Sarpkaya's hypothesis that the

discrepancy between measured and calculated drag values for $KC > 0{\cdot}7$ when β exceeds 1000 is the result of a three-dimensional instability, which cannot be investigated by a two-dimensional computation. Moreover, Skomedal *et al.*,[12] Graham and Djahansouzi[13] and Smith and Stansby[14] used discrete vortex methods for the calculation of two-dimensional flow. Skomedal *et al.*[12] employed the random walk method for the solution and compared their results with measurements in a U-tube under similar conditions. Although the flow pattern derived computationally was in good agreement with the experimental flow visualization, and the computed RMS values of the total in-line force compared reasonably with the measured ones in most cases, disagreement was observed between the computed and measured coefficients of the in-line force for $KC > 10$. In addition, discrepancies were detected between computed and measured RMS values of the transverse force. Graham and Djahansouzi[13] presented results of the flow pattern and force coefficients for $\beta = 196$ and $KC = 1$–6. Smith and Stansby[14] used the random vortex method for the solution of oscillating flow around cylinders. Their solution is confined to $KC \leqslant 3$, but apart from circular cylinders, they also examined cylinders of non-circular cross-section. Anagnostopoulos *et al.*[15] employed a finite element scheme for the solution of oscillating flow at $Re = 100$ and $KC = 2$ and 4 in the regime where the flow remains symmetrical.

In the present study the finite element method was used for the solution of viscous oscillatory flow around a circular cylinder. The computation was conducted at Keulegan–Carpenter numbers extending up to $KC = 15$ and frequency parameters between $\beta = 6$ and 100. The symmetrical flow regime was considered first, and afterwards the various vortex-shedding cases were studied. Emphasis was given to the analysis of asymmetric flows in the region where the frequency parameter was kept low, yielding Reynolds numbers lower than 500. The numerical solution provides a complete description of the flow field and the hydrodynamic forces exerted on the cylinder. Since the flow phenomenon is highly unsteady, the flow visualization patterns are presented at various time instants over one or one-half of an oscillation cycle when the flow is periodic, and at consecutive periods in the aperiodic flow regime. To confirm the validity of the computer code, the numerical results are compared with experimental flow visualizations and force measurements under similar conditions.

2. NUMERICAL SOLUTION

2.1. Governing equations

In the present study the streamfunction (Ψ) and vorticity (ζ) formulation of the Navier–Stokes equations was used, according to which

$$\nabla^2 \Psi = -\zeta, \tag{4}$$

$$\frac{\partial \zeta}{\partial t} + \frac{\partial \Psi}{\partial y}\frac{\partial \zeta}{\partial x} - \frac{\partial \Psi}{\partial x}\frac{\partial \zeta}{\partial y} = \nu \nabla^2 \zeta. \tag{5}$$

Considering the values of Ψ and ζ at two successive time levels n and $n+1$, the governing equations become

$$\nabla^2 \Psi_{n+1} = -\zeta_n, \tag{6}$$

$$\frac{\partial \zeta_n}{\partial t} + \frac{\partial \Psi_{n+1}}{\partial y}\frac{\partial \zeta_n}{\partial x} - \frac{\partial \Psi_{n+1}}{\partial x}\frac{\partial \zeta_n}{\partial y} = \nu \nabla^2 \zeta_{n+1}. \tag{7}$$

2.2. Boundary conditions

The time-dependent freestream velocity $U(t)$ of the oscillatory flow is defined in terms of the maximum flow velocity U_m as

$$U(t) = U_m \sin \phi, \qquad \phi = 2\pi t/T, \tag{8}$$

where t is the time interval considered from the inception of the flow oscillation. The boundary condition for the streamfunction on the horizontal boundaries U and D shown in Figure 1 is

$$\Psi_U = U(t)\, y_U, \qquad \Psi_D = U(t)\, y_D, \tag{9}$$

while on the vertical boundaries L and R the streamfunction varies linearly according to the relationship

$$\Psi = U(t)\, y. \tag{10}$$

As origin of the co-ordinate system, the intersection of the boundary L and the horizontal axis of symmetry of the solution domain was taken.

The vorticity was assumed equal to zero throughout the outer boundaries, while along a no-slip boundary it can be calculated from the formula

$$\zeta_1 = \frac{3 \int_S (u\, dx + v\, dy)}{\Delta} - (\zeta_2 + \zeta_3), \tag{11}$$

which is easily derived from the relationship between the vorticity and circulation over an element, and whose various parameters are explained in Figure 2. Here ζ_1, ζ_2 and ζ_3 are the vorticity values at the three nodes of the element (e) considered, and the two components of the fluid velocity along the element boundary are denoted as u and v. Δ is the area of the element, while the S appearing in the integral denotes integration around the whole perimeter of the element. The integration in (11) was conducted by expressing u and v in terms of the corresponding nodal velocities using linear interpolation.

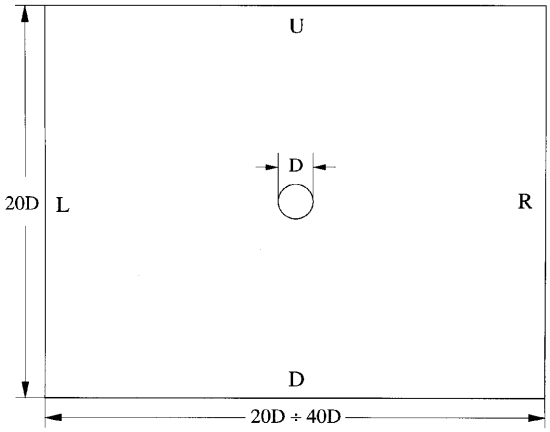

Figure 1. Solution domain

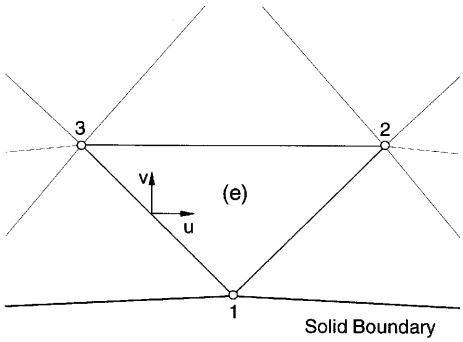

Figure 2. Definition sketch

2.3. Solution technique

A finite element technique was used for the solution, similar to that used by Smith and Brebbia[16,17] and Anagnostopoulos[18] for the solution of flow around cylinders in a uniform stream. The main features of the solution procedure are described as follows.

Assuming that $\Psi_{n+1}^{(e)}$ is the approximation of the streamfunction over the element (e) application of Galerkin's method to (6) yields

$$\int\int_{D^{(e)}} N_i^{(e)} \left(\frac{\partial^2 \Psi_{n+1}^{(e)}}{\partial x^2} + \frac{\partial^2 \Psi_{n+1}^{(e)}}{\partial y^2} + \zeta_n^{(e)} \right) \mathrm{d}x\, \mathrm{d}y = 0, \quad i = 1, 2, 3, \tag{12}$$

where $N_i^{(e)}$ are the interpolation functions for the element (e). Integrating equations (12), expressing $\Psi_{n+1}^{(e)}$ and $\zeta_n^{(e)}$ in terms of their nodal values for the element considered, as

$$\Psi_{n+1}^{(e)} = [N]^{(e)} \{\Psi\}_{n+1}^{(e)}, \qquad \zeta_n^{(e)} = [N]^{(e)} \{\zeta\}_n^{(e)}, \tag{13}$$

and assembling for the whole solution domain, we obtain the matrix relationship

$$[K_1]\{\Psi\}_{n+1} = [K_2]\{\zeta\}_n + \{R_1\}, \tag{14}$$

where $[K_1]$ and $[K_2]$ are square matrices and $\{R_1\}$ is a column matrix. Since $\partial\Psi/\partial n = 0$ throughout the boundaries, the matrix $\{R_1\}$ becomes equal to zero. Storage requirements are reduced considerably by taking advantage of the symmetric and banded character of the matrices $[K_1]$ and $[K_2]$.

In a similar manner, application of Galerkin's method to (7) yields

$$\begin{aligned} &\int\int_{D^{(e)}} N_i^{(e)} v \left(\frac{\partial^2 \zeta_{n+1}^{(e)}}{\partial x^2} + \frac{\partial^2 \zeta_{n+1}^{(e)}}{\partial y^2} \right) \mathrm{d}x\, \mathrm{d}y \\ &\quad = \int\int_{D^{(e)}} N_i^{(e)} \left(\frac{\partial \zeta_n}{\partial t} + \frac{\partial \Psi_{n+1}}{\partial y} \frac{\partial \zeta_n}{\partial x} - \frac{\partial \zeta_{n+1}}{\partial x} \frac{\partial \zeta_n}{\partial y} \right) \mathrm{d}x\, \mathrm{d}y, \quad i = 1, 2, 3. \end{aligned} \tag{15}$$

Integration of (15) and assembly throughout the domain yields the matrix relationship

$$[K_3]\{\zeta\}_{n+1} + [K_4]\{\dot{\zeta}\}_{n+1} + \{R_2\} = \{R_3\}, \tag{16}$$

where $\dot{\zeta}$ is the derivative of ζ with respect to time. The matrices $[K_3]$ and $[K_4]$ are stored in banded form for the reduction of storage requirements, whereas $\{R_2\}$ and $\{R_3\}$ are column matrices. Expressing $\dot{\zeta}$ as

$$\dot{\zeta}_{n+1} = \frac{\zeta_{n+1} - \zeta_n}{\Delta t},$$

equation (16) becomes

$$\left([K_3] + \frac{1}{\Delta t}[K_4]\right)\{\zeta\}_{n+1} = \frac{1}{\Delta t}[K_4]\{\zeta\}_n - \{R_2\}, \tag{17}$$

since the natural boundary condition for ζ is $\partial\zeta/\partial n = 0$, rendering the matrix $\{R_3\}$ equal to zero.

The solution is started assuming zero vorticity throughout the solution domain. The solution algorithm consists of the following steps.

1. The streamfunction is evaluated at time $t + \Delta t$ from the solution of (14) using the known nodal values of vorticity at time t.
2. The vorticity values at the no-slip boundary are corrected from (11).
3. The vorticity at $t + \Delta t$ is calculated from the solution of (17).

2.4. Computational mesh

For the solution of the problem, various computational meshes were used, the exact mesh configuration depending on the flow case under investigation. All meshes consist of three-node triangular elements, as shown in the sample of Figure 3. In the part of the solution domain near the cylinder where a refined grid was used, the nodal points were placed on circles concentric with the cylinder cross-section. The element size in the vicinity of the cylinder was very small, increasing gradually with the distance from the cylinder, as shown in the enlarged view near the cylinder appearing in the window. An important issue is the element size close to the cylinder compared with the boundary layer thickness δ of the oscillating flow. As a guideline, we used the boundary layer thickness around an oscillating flat plate (Stokes' second problem[6]), which can be approximated by $\delta \approx 4(\nu/\omega)^{1/2}$, where δ is defined as the distance from the plate at which u/U_m is 6% and ω denotes the circular frequency of oscillation. Assuming that the previous value of δ applies also for a circular cylinder and recalling the definition of the frequency parameter from (3), the previous relationship after some manipulation yields $\delta/D \approx 4/(2\pi\beta)^{1/2}$. Therefore this formula, showing clearly that the boundary layer thickness decreases with increasing square root of β, can be used as a guideline for the determination of δ. For $\beta = 100$ the ratio δ/D was found to be equal to 0·16, whereas for $\beta = 10$ the ratio δ/D equals 0·5.

From the previous discussion it is evident that for higher β-values a more refined grid near the cylinder should be used for better accuracy of the field variables within the boundary layer. The enlarged view of Figure 3 suggests that the grid refinement near the cylinder was adequate for the resolution of flow within the boundary layer in the range of β-values examined. The validity of applying the boundary layer thickness of oscillatory flow around a flat plate to oscillating flow around a circular cylinder will to be examined later, considering velocity profiles derived from the solution.

For the KC and β parameter values at which the phenomenon was symmetrical with respect to the wake centreline, a mesh with vertical boundaries (denoted as L and R in Figure 1) located 10 cylinder diameters upstream and downstream from the cylinder centre was used. For the KC and β parameter regime in which the flow was asymmetric with respect to the wake centreline, the boundaries L and R were located 20 diameters upstream and downstream from the cylinder centre. It is evident that since

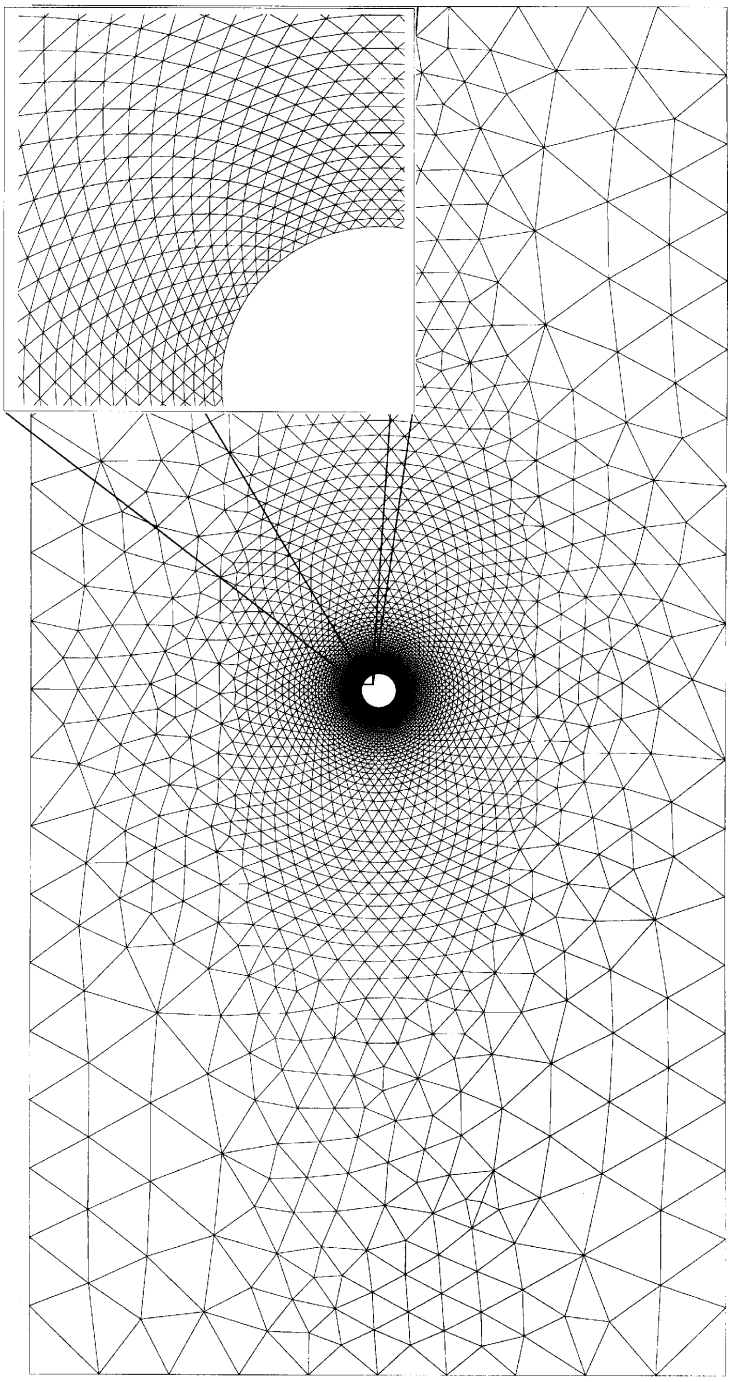

Figure 3. Finite element mesh

the extent of the symmetrical flow regime was not known *a priori*, when the solution of a flow case attempted with a shorter mesh became eventually asymmetric, it was continued with a grid network which encompassed a larger part of the flow field in the streamwise direction. The mesh of Figure 3, used for the study of asymmetric flow, contains 3352 nodes and 6580 elements. In most cases, 64 nodal points were placed on the cylinder boundary. In the exceptional case where the separation angle was under the investigation, the number of nodal points on the cylinder was increased to 128 for an improvement in the solution accuracy.

The upper and lower mesh boundaries (U and D of Figure 1) were placed 10 cylinder diameters above and below the wake centreline. Although a smaller distance between U and D would reduce the number of nodes contained in the computational grid, the distance of 20 diameters between boundaries U and D was favoured in order to simulate as accurately as possible the unrestricted flow conditions.

2.5. *Calculations of shear, pressure and forces*

The pressure distribution on the cylinder surface can be calculated from the relationship

$$\left(\frac{\partial p}{\partial s}\right)_{\mathrm{w}} = \rho v \left(\frac{\partial \zeta}{\partial n}\right)_{\mathrm{w}}, \tag{18}$$

where s and n are the tangential and normal directions on the cylinder surface at the point considered.

The pressure distribution throughout the flow field can be calculated from the solution of Poisson's equation:

$$\frac{\partial^2 p}{\partial x^2} + \frac{\partial^2 p}{\partial y^2} = -2\rho\left(\frac{\partial u}{\partial y}\frac{\partial v}{\partial x} - \frac{\partial u}{\partial x}\frac{\partial v}{\partial y}\right). \tag{19}$$

Application of Galerkin's method to (19) for an element (e) and assembly throughout the domain as described by Anagnostpoulos[18,19] yields

$$[K_5]\{p\} = \{R_4\} + \{R_5\}, \tag{20}$$

in which the element r_{5i} of the column matrix $\{R_5\}$ is given by

$$r_{5i} = \int_S \frac{\partial p}{\partial n}\, \mathrm{d}s. \tag{21}$$

The integration is performed at the part of the boundary where a natural boundary condition for pressure is specified. The equation of motion along the radial direction on the cylinder surface yields the following boundary condition for pressure on the cylinder:

$$\frac{\partial p}{\partial n} = \mu \frac{\partial \zeta}{\partial s}. \tag{22}$$

On the other hand, the equation of motion in the horizontal direction on the boundaries L and R of Figure 1, where the vorticity is zero, yields the boundary condition for pressure as

$$\frac{\partial p}{\partial n} = -\rho \frac{\mathrm{d}U}{\mathrm{d}t}, \tag{23}$$

where U is the time-dependent stream velocity given by (8).

It is evident that equation (18) gives the pressure distribution only around the cylinder, whereas Poisson's equation yields the pressure distribution throughout the solution domain. For the evaluation of pressure throughout the solution domain, the system of equations (20) should be solved, which is computationally more expensive than the direct application of (18).

The shear stress on the cylinder was calculated from the vorticity ζ_w at the boundary by the formula

$$\tau_w = -\mu\zeta_w. \tag{24}$$

The in-line and transverse forces per unit cylinder length are calculated from the integration of shear and pressure around the cylinder as

$$F_x^* = \int_0^{2\pi} p\cos\theta \, d\theta - \mu \int_0^{2\pi} \zeta_w \sin\theta \, d\theta, \tag{25}$$

$$F_y^* = -\int_0^{2\pi} p\sin\theta \, d\theta - \mu \int_0^{2\pi} \zeta_w \cos\theta \, d\theta, \tag{26}$$

where θ is the angle defining the location of the point considered from the leading edge of the cylinder in the clockwise direction. F_x^* and F_y^* can be non-dimensionalized according to the formulae

$$F_x = F_x^*/0{\cdot}5\rho U_m^2 D, \qquad F_y = F_y^*/0{\cdot}5\rho U_m^2 D. \tag{27}$$

3. RESULTS

Computations of oscillating flow around a circular cylinder have been conducted for a large number of pairs of KC and β, for KC extending up to 15 and β ranging between 6 and 100. Results of symmetrical flow will be presented first in terms of the flow pattern and time-dependent hydrodynamic forces. Similar sets of results will be used in the asymmetric flow regime for the interpretation of the various vortex-shedding patterns. The force coefficients derived from the total in-line force will be presented for $\beta = 34$ and 53 in the interval $0 < KC < 10$. An important issue of the whole study is the boundary between symmetrical and asymmetric flow, which can be determined on the KC–β plane from the results of the various flow cases.

Formula (3) dictates that in the present study the Reynolds number may exceed 500, therefore a matter of interest is the range over which the present laminar code can fully resolve the flow; it should be remembered that in the case of steady flow around a circular cylinder the transition to turbulence is initiated for Re between 150 and 200. Sarpkaya[3] reports that the KC at which the oscillating flow around a cylinder becomes turbulent decreases with increasing values of the frequency parameter. At $\beta = 125$, which is the lowest value he considered, the KC_t at which the boundary layers become turbulent is 3·25, while the projection of the data line at lower β-values would give $KC_t = 4$ for $\beta = 50$. It seems therefore that in the set of computations for $\beta = 53$ the present laminar code can fully resolve the flow for $KC < 4$. For $KC > 4$ it will be assumed that the flow remains laminar in the largest part of the oscillation cycle where $U(t)$ is lower than U_m, therefore the error from the use of the present code can be considered as small. A similar assumption is made for the higher KC-values considered herein when $\beta = 34$.

3.1. Symmetrical flow

Boundary between symmetrical and asymmetric flow. It is well known from previous studies that at low KC the flow remains symmetrical with respect to the wake centreline. Bearman *et al.*[1] and Williamson[2] report that symmetrical pairing of vortices occurs for $KC < 4$. The visual study by Tatsuno and Bearman[4] and Justesen's[11] computations revealed that the KC at which the inception of asymmetric flow is observed depends also on β.

The evaluation of the KC above which asymmetric flow occurs for a certain β was conducted with the technique described as follows. For each pair of KC and β under examination, disturbances to the flow were introduced artificially, accomplished by increasing the vorticity at some nodal points close to the wake centreline upstream and downstream from the cylinder. In the case where these disturbances were amplified, leading to complicated vortex-shedding patterns, the flow was characterized as asymmetric, while their dampening suggested the persistence of symmetrical flow. It should be stressed that the asymmetries in the vortex-shedding cases could be developed without the introduction of disturbances, but in such a case the process was much slower, requiring a large number of oscillation cycles, especially for values of KC–β lying close to the boundary with the symmetrical flow.

After a series of tests with a large number of KC and β pairs as shown in Figure 4, the boundary between symmetrical and asymmetric flow on the KC–β plane was determined in the form of a fitting curve. It should be added that even in the case of symmetrical flow, small-scale asymmetries were detectable in the flow field above and below the wake centreline, giving rise to a very small transverse force. These asymmetries were also observed by Smith and Stansby,[14] who used an enforced symmetry technique for their elimination. It is evendent that the KC at which the asymmetry of flow begins decreases drastically with increasing values of the frequency parameter. The inception of asymmetry occurs at $KC \approx 10{\cdot}5$ for $\beta = 10$, whereas the flow becomes asymmetric at $KC = 3{\cdot}5$ for $\beta = 100$. The decrease in the critical KC marking the boundary between symmetrical and asymmetric flow is very abrupt at low β-values. Figure 4 shows that good agreement exists with the results of the visual study by Tatsuno and Bearman,[4] although for the same value of β the critical KC in the experiment is somewhat lower than that derived from the computation. The difference is more pronounced in the low β-value regime.

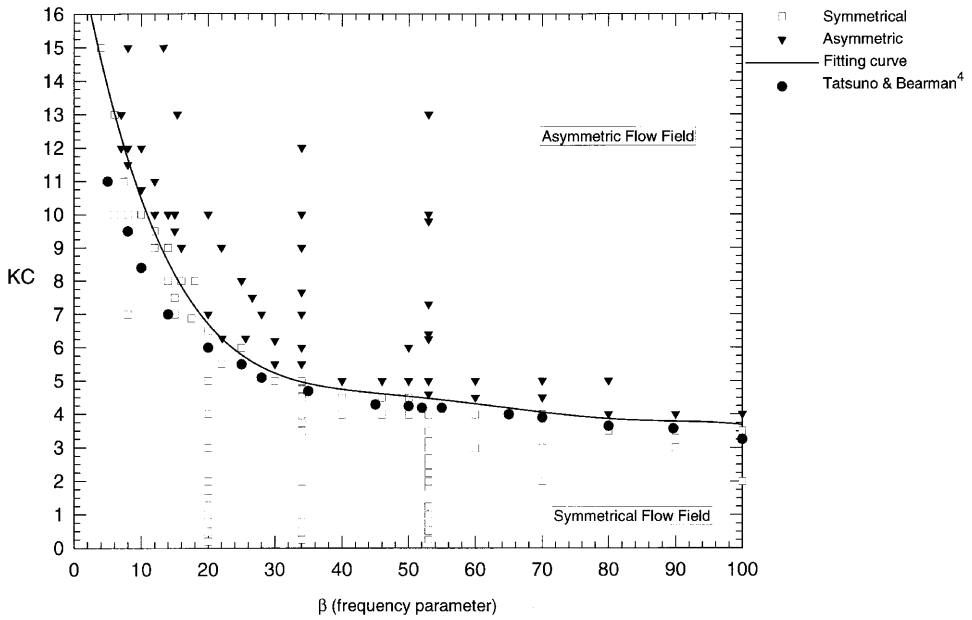

Figure 4. Boundary between symmetrical and asymmetric flow

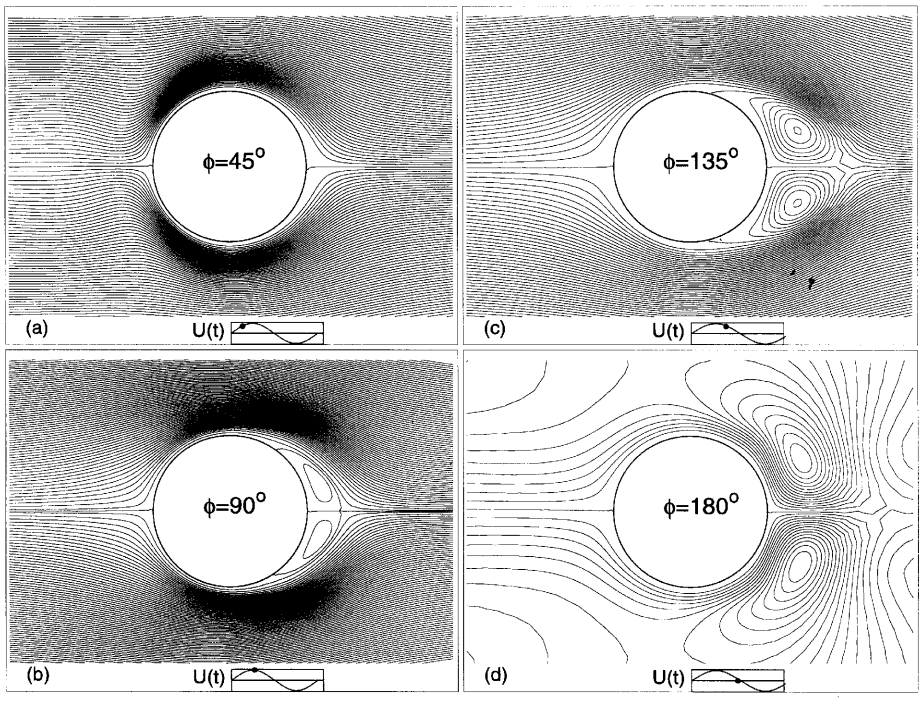

Figure 5. Streamline patterns over one-half of an oscillation cycle for $KC = 4$ and $\beta = 50$

Flow pattern. The streamlines with respect to a stationary frame of reference during one-half of an oscillation cycle for $KC = 4$ and $\beta = 50$ ($Re = 200$) are depicted in Figure 5. Four flow patterns are presented for the half-cycle during which the freestream velocity is positive ($0^\circ \leqslant \phi \leqslant 180^\circ$). The sequence of frames reveals that a symmetrical pair of counter-rotating vortices is formed behind the cylinder during each half-cycle, whose size increases with the phase angle. It is interesting to observe the curvature of streamlines upstream from the cylinder in Figure 5(a), owing to the vorticity generated during the previous half-cycle. This feature is in contradiction to the flow pattern around a cylinder in unidirectional flow.

For the investigation of the effect of the change in direction of the approaching velocity, six streamline patterns have been plotted in Figure 6 for the case $KC = 4$ and $\beta = 50$, for ϕ around 180°. Figure 6 shows that as ϕ increases towards 180°, the two separation bubbles above and below the wake centreline increase in size and encroach upon a large part of the flow field upstream from the cylinder, until they are split into two parts each. When ϕ becomes almost equal to 180°, a second pair of counter-rotating vortices is detectable behind the cylinder. As the fluid velocity changes direction, the two vortex pairs formed behind the cylinder decrease in size continually, until they finally disappear.

The equivorticity lines for $Re = 200$ and $KC = 2$ and 4 ($\beta = 100$ and 50 respectively) are displayed in Figure 7. Throughout the present work the vorticity has been non-dimensionalized according to the formula $\zeta^* = \zeta D/2U_m$. Moreover, the positive values of vorticity and pressure contours will be sketched with full lines and the negative values with broken lines. In the case where $KC = 2$, at $\phi = 0^\circ$ the vorticity is negative in the upper half of the cylinder and positive in the lower half. A pair of vorticity contours can be seen upstream from the cylinder, of positive and negative vorticity above

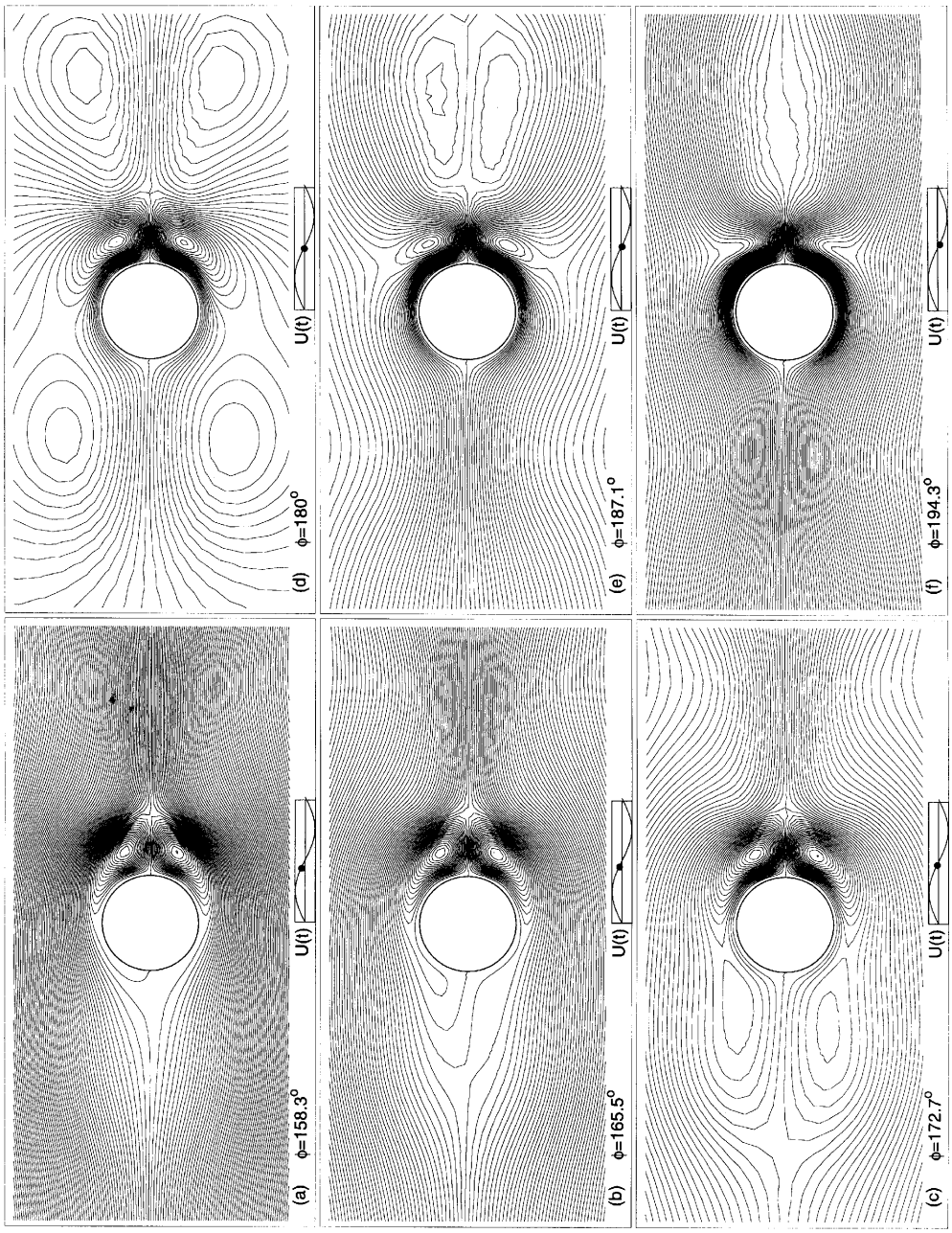

Figure 6. Streamline patterns for phase angle around 180°; $KC = 4$ and $\beta = 50$

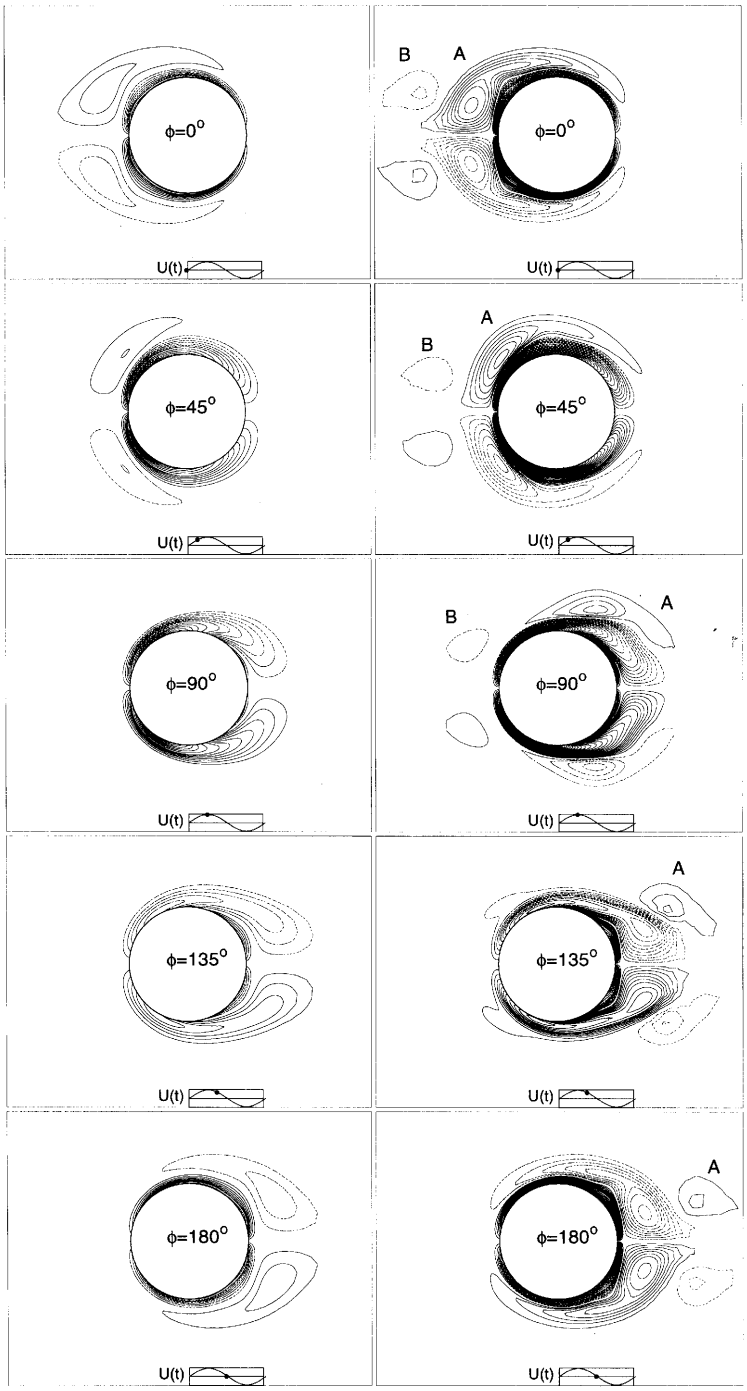

(I) (II)

Figure 7. Vorticity contours over one half-cycle: (I) $KC = 2$ and $\beta = 100$; (II) $KC = 4$ and $\beta = 50$. The full lines represent positive and the broken lines negative values of vorticity

and below the wake centreline respectively. These vorticity contours have been reduced in size for $\phi = 45^\circ$ and disappeared for $\phi = 90^\circ$. For $\phi = 90^\circ$, positive vorticity is detectable in the downstream part of the cylinder above the wake centreline and negative vorticity below the wake axis. As ϕ becomes greater than 90°, the positive vorticity area above the wake centreline is extended, until it reaches the leading edge of the cylinder at $\phi = 180^\circ$; the behaviour of the negative vorticity below the wake axis is similar. When KC is increased to 4, at $\phi = 0^\circ$ we can see two pairs of opposite sign vorticity contours upstream from the cylinder, generated during the previous half-cycle, the pair A close to the cylinder and the pair B further upstream. The streamline curvature upstream from the cylinder quoted before can be explained with reference to this vorticity distribution. As the flow direction reverses, these two pairs of vorticity loops are washed downstream. The pair B, which moves slowly towards the cylinder, is still detectable at $\phi = 90^\circ$ and amalgamates with the vorticity generated on the cylinder when ϕ becomes equal to 135°. The pair A, although it decreases in size from the interaction with the vorticity generated on the cylinder as it is convected downstream, persists and is still detectable at $\phi = 180^\circ$.

In Figure 8 the length of the separation bubble as a function of the phase angle is depicted for $Re = 200$ and $KC = 2$ and 4. The length of the separation bubble increases almost linearly with the phase angle for $\phi < 160^\circ$ when $KC = 2$, and throughout the half-cycle for $KC = 4$. Figure 8 dictates that for equal phase angles the separation bubble becomes larger with increasing KC, a result quoted also by Justesen[11] in the same range of KC for $\beta = 250$. Comparison with Justesen's results reveals that for constant KC the separation bubble decreases with increasing β.

The distribution of the dimensionless vorticity around the upper half of the cylinder for $\beta = 50$ and $KC = 4$ ($Re = 200$) over one half-cycle is shown in Figure 9. For $\phi = 0^\circ$ the maximum absolute vorticity occurs close to the leading edge of the cylinder. The maximum absolute vorticity increases as the phase angle is increased to 45°, while for $\phi = 135^\circ$ the absolute vorticity values around the cylinder become low. When ϕ has reached 90°, a positive vorticity region can be seen in the downstream part of the cylinder where the flow has been separated, in agreement with the vorticity distribution of Figure 7.

The profiles of the streamwise velocity along the vertical axis through the cylinder centre are displayed in Figure 10 for four different KC–β pairs in the symmetrical flow regime. In all four cases the thickness of the boundary layer will be compared with that of an oscillating flat plate when the phase angle is equal to zero, implying zero instantaneous stream velocity. For the three β-values examined, the boundary layer thickness on an oscillating flat plate is: (a) $\beta = 100$, $\delta/R = 0{\cdot}32$; (b) $\beta = 50$, $\delta/R = 0{\cdot}46$; (c) $\beta = 7{\cdot}4$, $\delta/R = 1{\cdot}18$. Recalling that the boundary layer thickness δ corresponds to streamwise velocity 6% of U_m, the values of δ/R obtained from Figure 10 are: (a) $KC = 2$ and $\beta = 100$, $\delta/R = 0{\cdot}29$; (b) $KC = 1$ and $\beta = 50$, $\delta/R = 0{\cdot}36$; (c) $KC = 4$ and $\beta = 50$, $\delta/R = 0{\cdot}50$; (d) $KC = 11$ and $\beta = 7{\cdot}4$, $\delta/R = 1{\cdot}34$. From the two different values of δ in cases (b) and (c) we conclude that although the boundary layer thickness in the case of the oscillating flat plate depends only on β, in the two-dimensional flow case around a cylinder it is also a function of KC. Moreover, the δ-values derived from Figure 10 differ from those predicted from the flat plate theory by 10%, except for $KC = 1$ and $\beta = 50$ where the discrepancy is higher. In spite of this discrepancy, the previous analysis has confirmed that the boundary layer thickness corresponding to oscillatory flow around a flat plate can be used for a first estimate of δ in the case of oscillating flow around a cylinder. For higher values of the phase angle the velocity profiles are different from those corresponding to $\phi = 0^\circ$. An interesting matter is the comparison of the velocity profiles when $\phi = 90^\circ$ in cases (a) and (c), which both yield a Reynolds number equal to 200. The superposition of the two profiles indicates almost perfect coincidence. This result can be explained by bearing in mind that when $\phi = 90^\circ$, the acceleration of the oscillating stream is zero, therefore the flow is dominated by the Reynolds number.

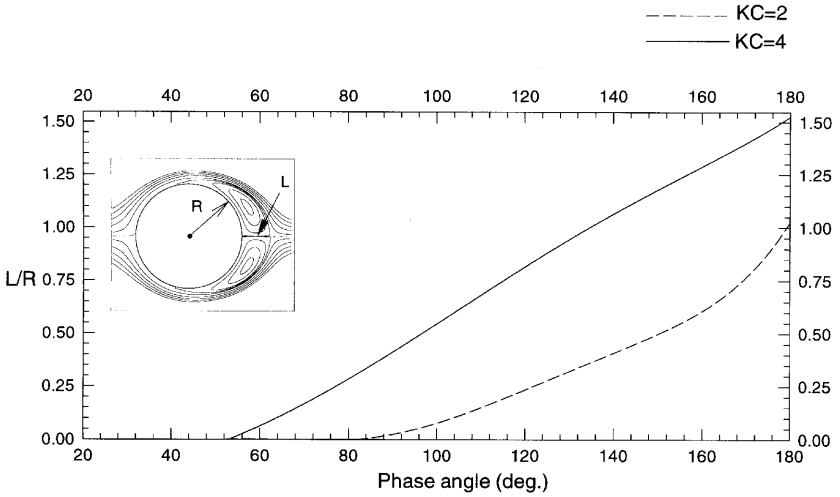

Figure 8. Length of separation bubble as a function of phase angle for $Re = 200$

Hydrodynamic force. For the evaluation of the pressure distribution around the cylinder the two techniques mentioned previously were tested, namely the application of equation (18) and the solution of the system of equations (20). The comparison of the results obtained from the two techniques was very good. Although the application of (18) is more economic, the solution of Poisson's equation was favoured in the present computation, since the complete pressure distribution throughout the solution domain was desirable. In the present context the pressure has been nondimensionalized according to the formula $p^* = p/0{\cdot}5\rho U_m^2$.

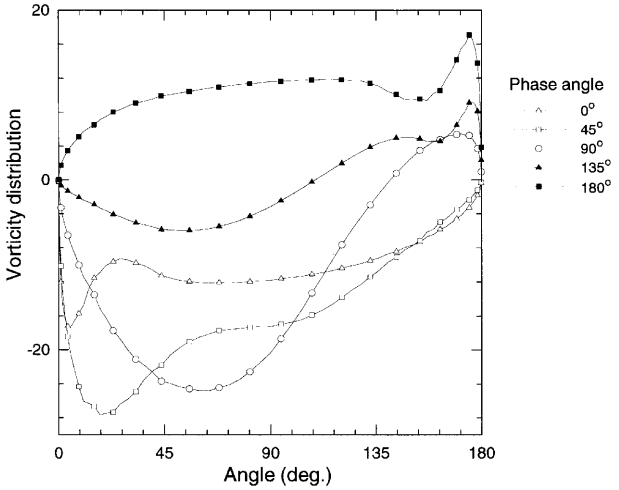

Figure 9. Vorticity distribution around cylinder over one half-period for $KC = 4$ and $\beta = 50$

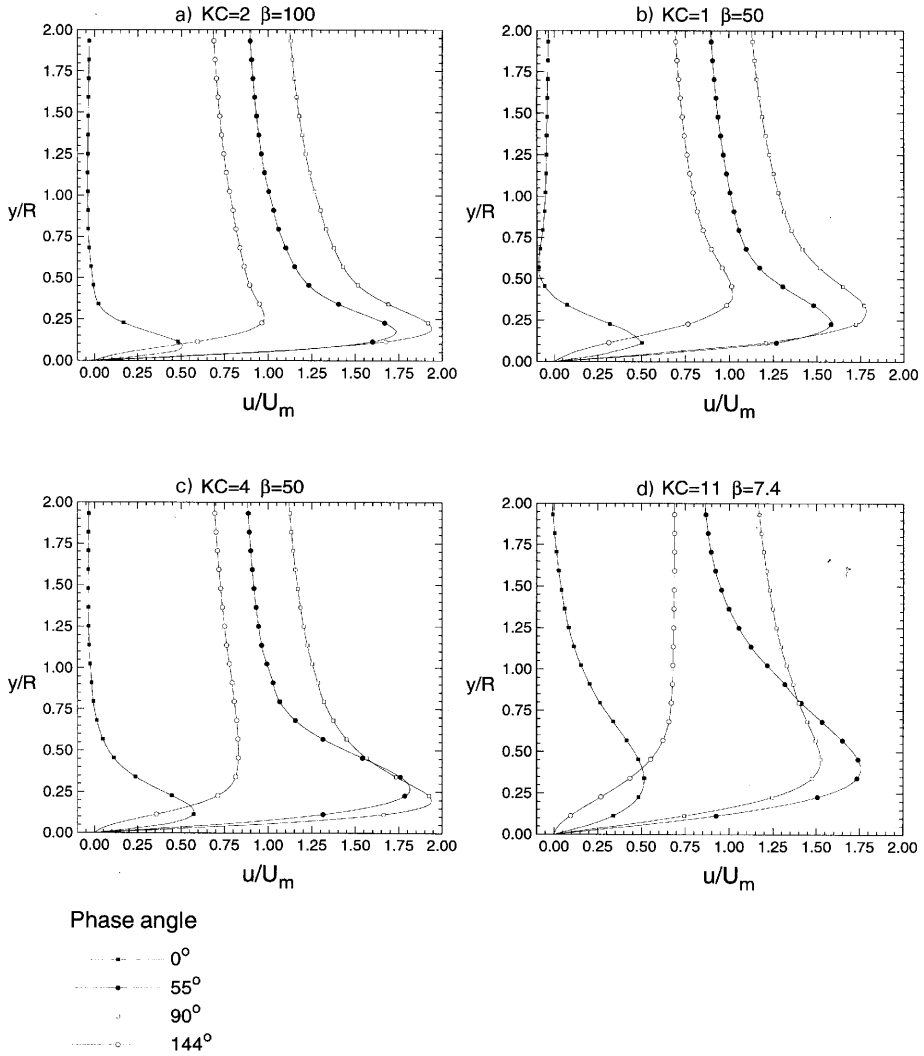

Figure 10. Profiles of streamwise velocity along vertical axis through cylinder centre for various values of KC and β

The total in-line force exerted on the cylinder was calculated from (25). The time history of the dimensionless in-line force for $KC = 2$ and $\beta = 100$ ($Re = 200$) is shown in Figure 11. Figure 11 reveals that the total force and its pressure and friction parts are almost sinusoidal and that the contribution of pressure to the total force is much greater than that of shear. Moreover, the freestream velocity lags behind the pressure force by approximately 90° and the shear force by 45°.

3.2. *Vortex-shedding cases*

If the Keulegan–Carpenter number exceeds a critical value which depends on the frequency parameter, asymmetries appear in the flow pattern which are eventually amplified and lead to complicated vortex-shedding patterns. As described in the Introduction, the existence of distinct vortex-shedding regimes is well established. Various attempts to study numerically these complicated

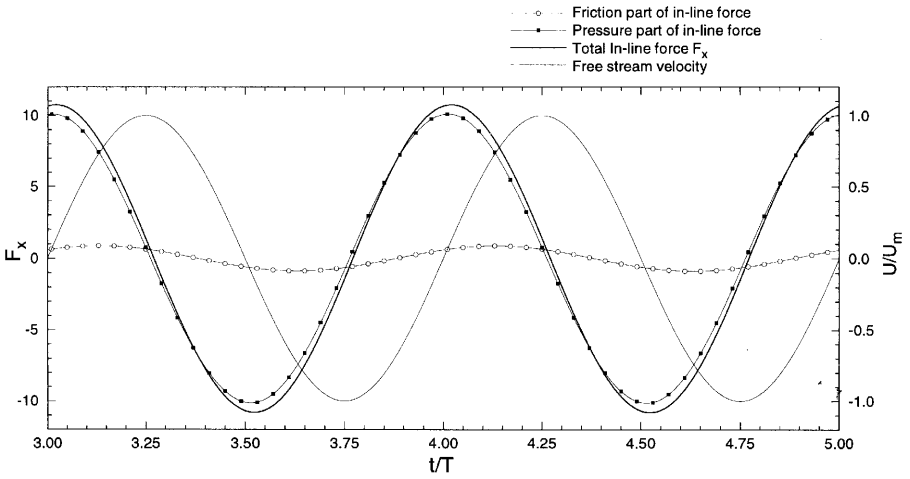

Figure 11. Time history of total in-line force and its components for $KC = 2$ and $\beta = 100$

flow patterns have been conducted for $\beta \geqslant 196$,[9–13] while only Wang and Dalton[10] quote computational results at low β-values. Since the visual study by Tatsuno and Bearman[4] revealed the existence of shedding patterns different from those observed at higher β-values, it was decided to confine the present solution to the range of β-values studied by those investigators. On a large part of the KC–β plane the flow is periodic, the periodicity being confirmed from the flow pattern and force traces. In addition, the numerical solution revealed the existence of an extensive regime on the KC–β plane in which the flow is aperiodic. This means that the flow pattern switches between different modes in consecutive cycles. For a better interpretation of this regime, which proved a very tempting issue, analysis of the flow pattern and force traces over a large number of consecutive cycles is required.

Oblique vortex rows. An example of oscillatory flow where asymmetries have been developed is given in Figure 12 for $KC = 6{\cdot}28$ and $\beta = 22{\cdot}1$, in which the equivorticity lines over one oscillation cycle are portrayed. Figure 12(a) depicts the vortices existing from previous cycles. The negative sign vortex in the lower part of the cylinder appears in elongated form compared with that formed at the upper side and is tilted upwards. In addition, two parallel rows of opposite sign vortices exist at both sides of the cylinder, inclined to the horizontal. The strength of these vortices decreases with increasing distance from the cylinder. For freestream velocity from left to right, negative vorticity develops in the upper half of the cylinder and positive vorticity in the lower half, whereas the vortices formed during previous cycles are convected towards the streamwise direction. It is seen from Figure 12(b) that the positive vorticity formed during the previous half-cycle above the cylinder starts to split into two parts, a process leading to the formation of two equal sign vortices in subsequent frames. The negative vortex formed during the previous half-cycle below the cylinder is swept downstream and pairs up with the opposite sign vortex forming below the cylinder. When the stream velocity becomes zero at $\phi = 180^\circ$, the negative sign vortex has moved further downstream, while the positive vortex forming below the cylinder appears in elongated form with respect to that forming above the cylinder, as shown in Figure 12(f). When the direction of the stream velocity reverses, the vortices shed during the previous half-cycle are swept back towards the cylinder, as shown in the sequence of frames in Figures 12(g)–12(j). Examination of the sequence of vorticity contours over the entire period indicates that one vortex is shed during each half-cycle. The solution over a large

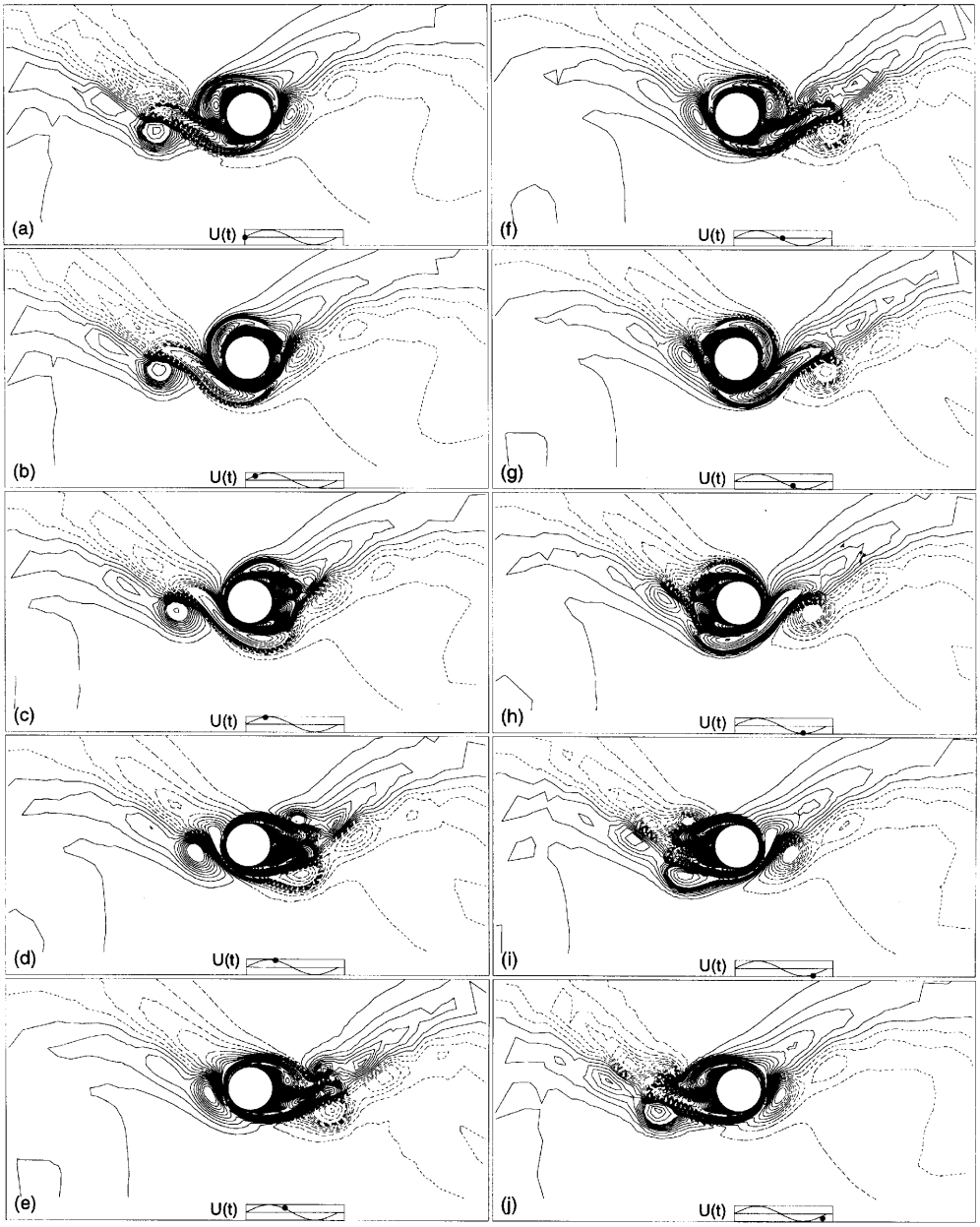

Figure 12. Vorticity contours over one oscillation cycle for $KC = 6{\cdot}28$ and $\beta = 22{\cdot}1$

number of oscillation cycles revealed the absolute periodicity of the phenomenon. The vorticity pattern of Figure 12 is in good agreement with the visual study by Tatsuno and Bearman[4] under similar conditions, characterized by those authors as regime 'D'.

Another solution was obtained for $KC = 6{\cdot}28$ and $\beta = 25{\cdot}6$, a case studied also by Tatsuno and Bearman.[4] The equivorticity lines for this case are depicted in Figure 13. The flow pattern is similar

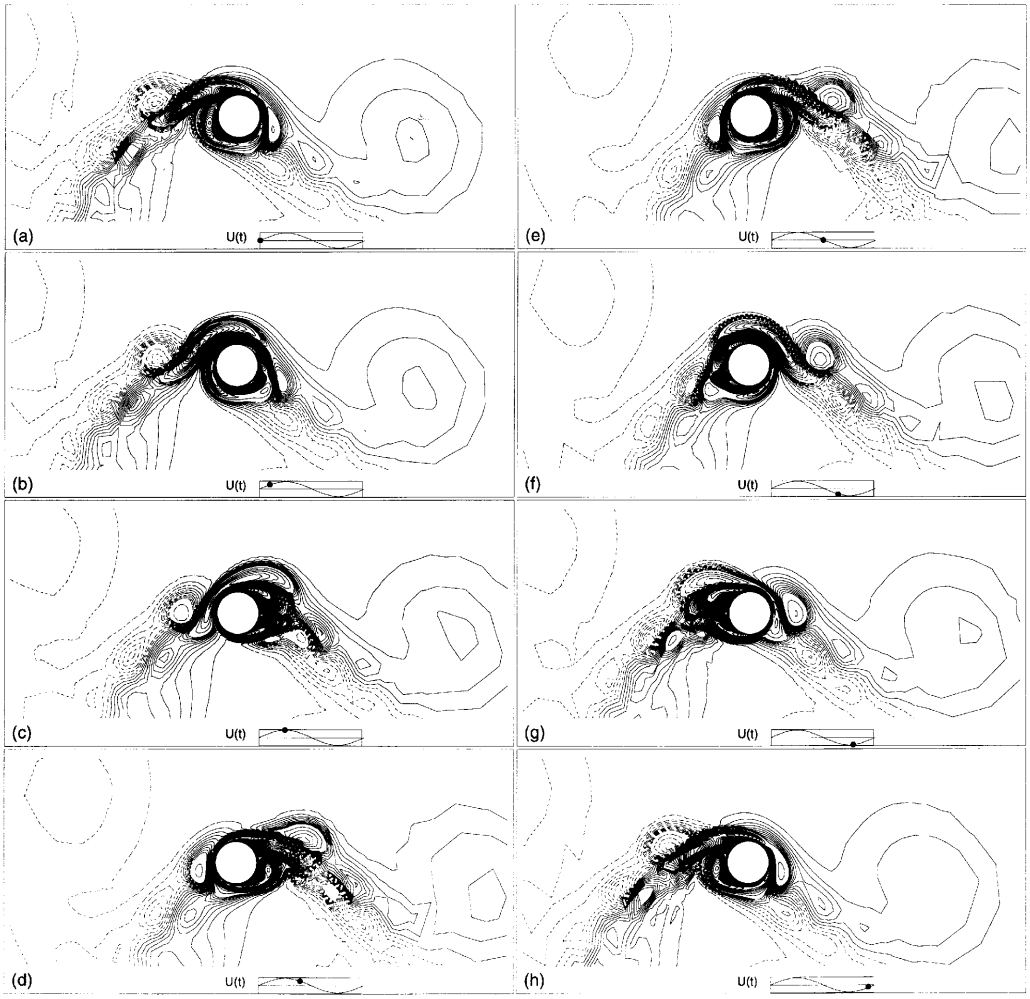

Figure 13. Vorticity contours over one oscillation cycle for $KC = 6{\cdot}28$ and $\beta = 25{\cdot}6$

to that of Figure 12, the main difference being the direction in which the vortices are aligned. Tatsuno and Bearman state that the flow which convects to one side of the axis of oscillation intermittently changes its direction to the other side. Moreover, their visual study revealed that this flow regime has a strong three-dimensional structure. The change in the flow direction led Tatsuno and Bearman to the classification of a new flow regime, denoted as 'E'. The solution over a large number of cycles did not show the switching of the flow direction observed experimentally. It seems therefore that the switching of the flow direction is associated with the three-dimensional character of the flow, whose solution is out of reach with the present two-dimensional code.

The time-dependent in-line force for $KC = 6{\cdot}28$ and $\beta = 25{\cdot}6$ is shown in Figure 14. The in-line force is periodic but not sinusoidal, a result compatible with the periodicity and asymmetry of the flow pattern. The asymmetry of the flow pattern with respect to the wake centreline gives rise to the generation of a transverse force, whose time history is also depicted in Figure 14. At the beginning of the cycle ($t/T = 25$) the transverse force has a low negative value. In the early stages of the cycle

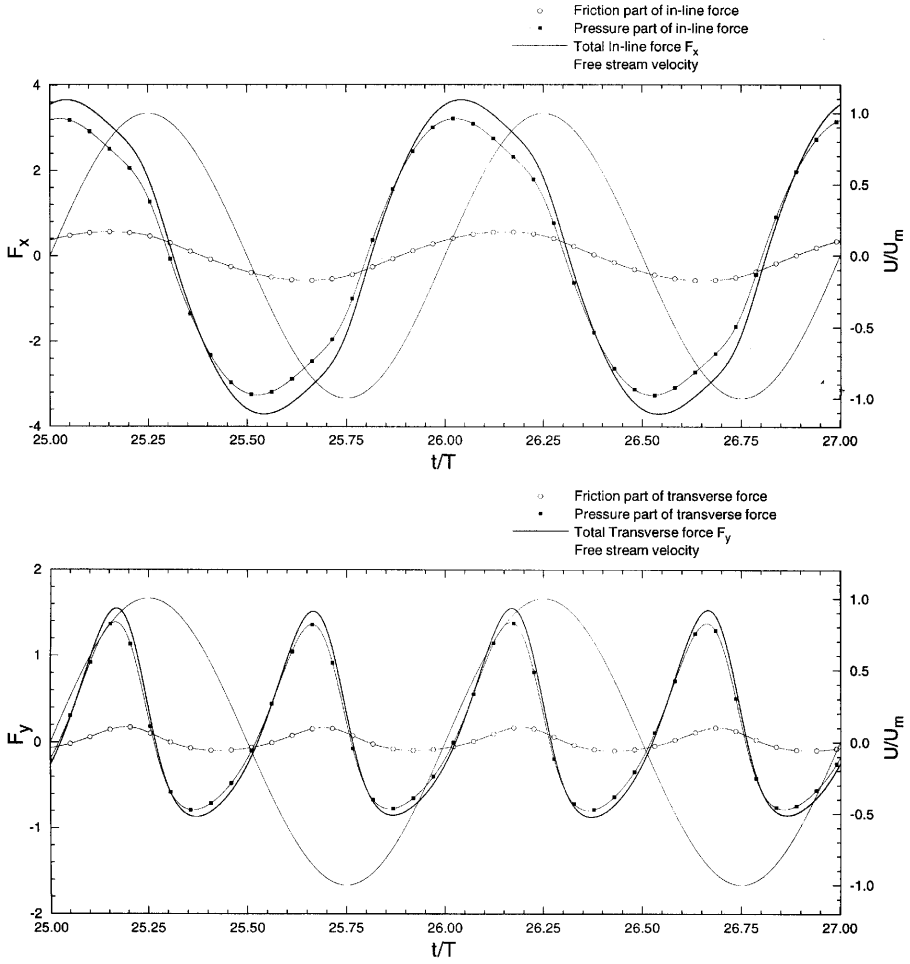

Figure 14. Traces of hydrodynamic forces during two oscillation periods for $KC = 6{\cdot}28$ and $\beta = 25{\cdot}6$

there is a surplus of negative vorticity on the cylinder surface, which is the reason for the positive peak of the transverse force at $\phi \approx 45^\circ$. This is analogous to the ideal flow case, where the superposition of a negative (clockwise) vortex on the uniform flow past a cylinder creates a positive lift force. At $\phi = 90^\circ$ the symmetry of the vortices attached above and below the cylinder depicted in Figure 13(c) results in zero transverse force, whereas the positive vorticity surplus below the cylinder in Figure 13(d) gives rise to a negative transverse force in the second quarter of the cycle. There exist two peaks per half cycle, therefore the frequency of the transverse force is twice the frequency of the oscillatory flow.

Double pair. Numerical experiments revealed that there exists a regime on the KC–β plane in which a vortex-shedding pattern occurs, according to which two pairs of counter-rotating vortices are shed per oscillation cycle. An example is the sequence of Figure 15, in which the vectors representing the relative fluid velocities with respect to the instantaneous stream velocity over one cycle are depicted for $KC = 10$ and $\beta = 20$. Three pairs of counter-rotating vortices existing from the previous

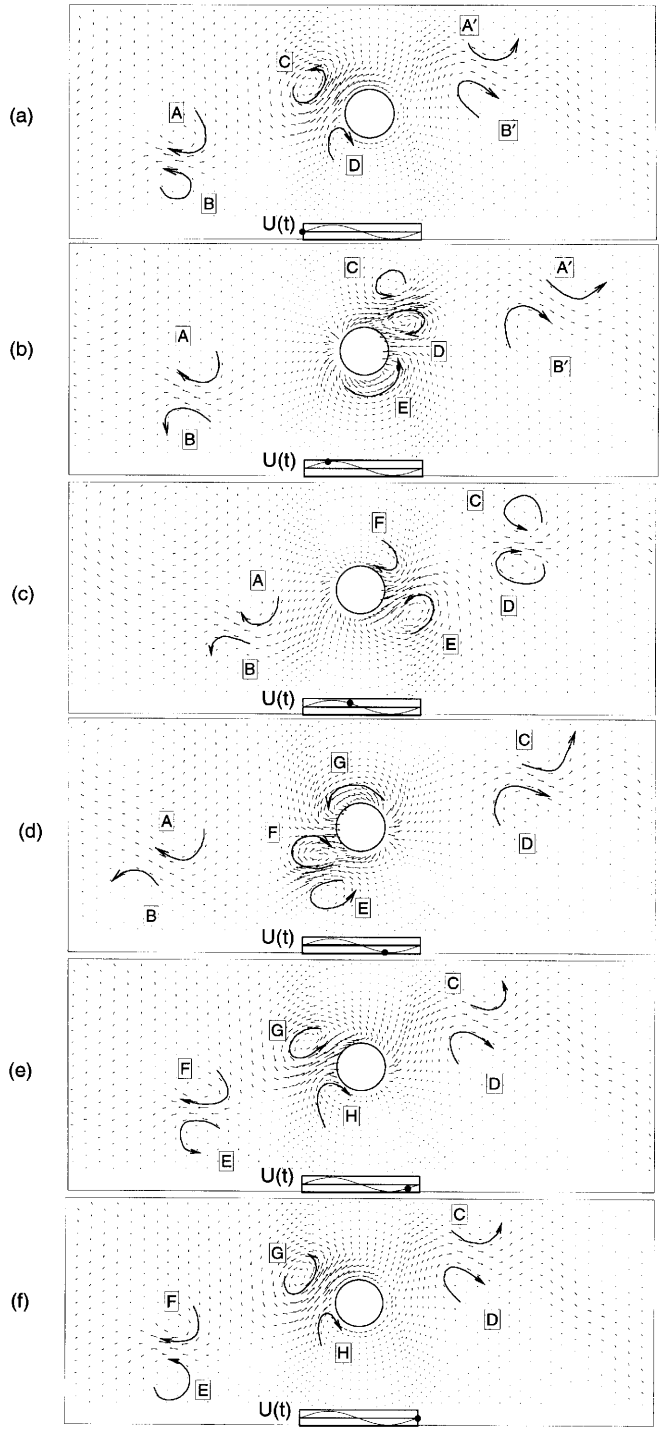

Figure 15. Velocity vectors and vortex patterns over one period for $KC = 10$ and $\beta = 20$. The frame of reference is that of a cylinder oscillating in still water

cycle are superimposed on the velocity field in Figure 15(a). The pair A′–B′ was shed during the first half of the previous cycle, whereas the pair A–B was shed during the second half. The vortices C and D close to the cylinder were formed during the previous half-cycle. As the flow direction reverses, the vortex D passes over the cylinder and pairs up with the vortex C, while the vortex E is forming below the cylinder, as shown in Figure 15(b). Each of the counter-rotating vortices C and D induces in the other a convective velocity towards the streamwise direction, which, superimposed on that of the oscillating stream, results in an increased velocity of the pair; this is the reason for the large displacement of the pair C–D between Figures 15(b) and 15(c). In Figure 15(c) the vortex F has been formed above the cylinder, while the pair C–D has been shed; the pair A′–B′ has moved further downstream, outside of the part of the solution domain displayed. As the flow velocity reverses, the vortex F passes below the cylinder and pairs up with the counter-rotating vortex E, as shown in Figure 15(d). The pair E–F has been shed in Figure 15(e), while the pair A–B has been swept in the direction of the stream velocity and is not visible any more. Therefore two pairs of counter-rotating vortices (C–D and E–F) are shed during an oscillation cycle.

The equivorticity lines, relative streamlines and isobars over one half-cycle are displayed in Figure 16. The contours of Figure 16 can be used for the exact determination of the instantaneous position of the centre of each vortex and provide an alternative for the interpretation of the shedding process explained previously with reference to Figure 15. The isobars of Figure 16(c) superimposed on the equivorticity lines at the same instant are displayed in Figure 17. It can be clearly seen that minimum pressure occurs at the centre of each vortex, whereas there exists a pressure hill at the point where the vorticity contours emerging from the cylinder and encompassing the vortex D come close to each other, forming a 'neck'. This pressure hill may be used for the definition of the vortex boundary, in a similar manner to the vortex shedding behind a cylinder in unidirectional flow, as has been shown in the numerical flow visualization study conducted by Anagnostopoulos.[19]

For the determination of the position of the vortices shed at previous cycles, the relative streamlines and vorticity contours over a larger part of the solution domain are presented in Figure 18. It is interesting to note that the vortices shed at subsequent cycles remain in close contact with each other, whereas the vortex strength is reduced as the distance from the cylinder increases. The present computational results compare very well with Tatsuno and Bearman's[4] flow visualization study in regime 'F'.

The pressure distribution around the cylinder at four time instants over one half-cycle is presented in Figure 19. When the arrows point inwards, the pressure is positive; when they point outwards, the pressure is negative. The values of the non-dimensional pressure around the cylinder are displayed on the diagrams, while the arrow in the cylinder indicates the magnitude and direction of the resulting pressure force.

The in-line and transverse forces are presented in Figure 20 over two oscillation cycles. Both forces are completely periodic. The maximum in-line force is lower than in the case of Figure 14 and occurs at $\phi = 56^\circ$. The clockwise vortex D of Figure 15 passing over the cylinder is the reason for the positive transverse force in the early stages of the cycle, whereas the counter-clockwise vortex E below the cylinder in Figure 15(b) results in negative transverse force for $\phi \approx 90^\circ$. The clockwise vortex F passing below the cylinder in Figures 15(c) and 15(d) induces negative transverse force in the early stages of the second half-period, whereas the counter-clockwise vortex G passing over the cylinder at $\phi = 170^\circ$ is the reason for the positive peak of the transverse force appearing in Figure 20 at $t/T \approx 20{\cdot}75$. The time history of the transverse force derived from the present computation is similar to that presented by Williamson[2] for a double pair when KC lies between 15 and 24 for increased values of β compared with those of the present study. In both cases the frequency of the transverse force is three times the oscillation frequency. Williamson states that the fundamental lift frequency is $n+1$ times the oscillation frequency, where n is the number of vortices shed per half-

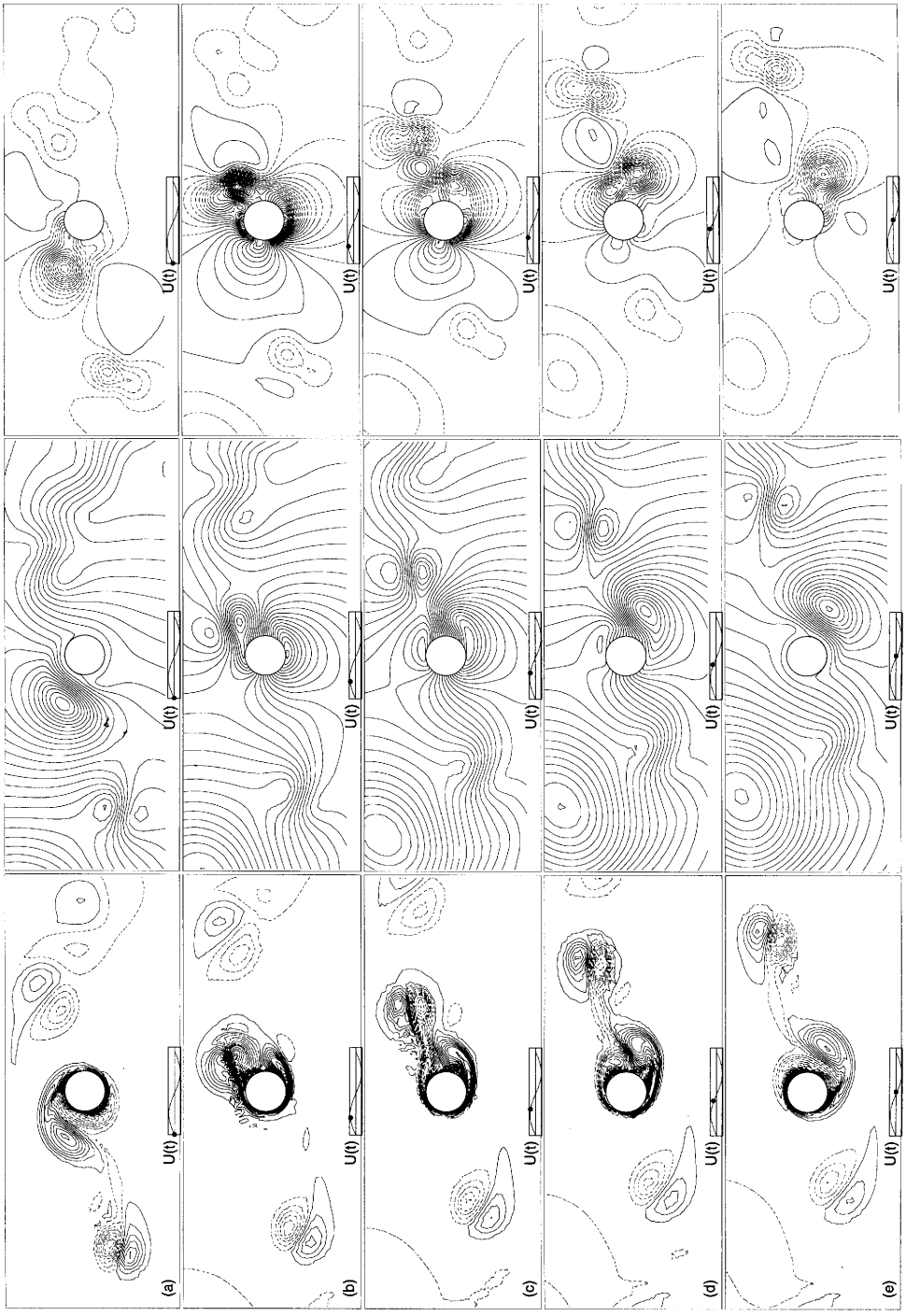

Figure 16. Flow field for $KC = 10$ and $\beta = 20$ over one-half of a period: (I) equivorticity lines; (II) streamlines, in a frame of reference with respect to oscillating stream velocity; (III) pressure contours. The full lines represent positive and the broken lines negative values in the vorticity and pressure diagrams

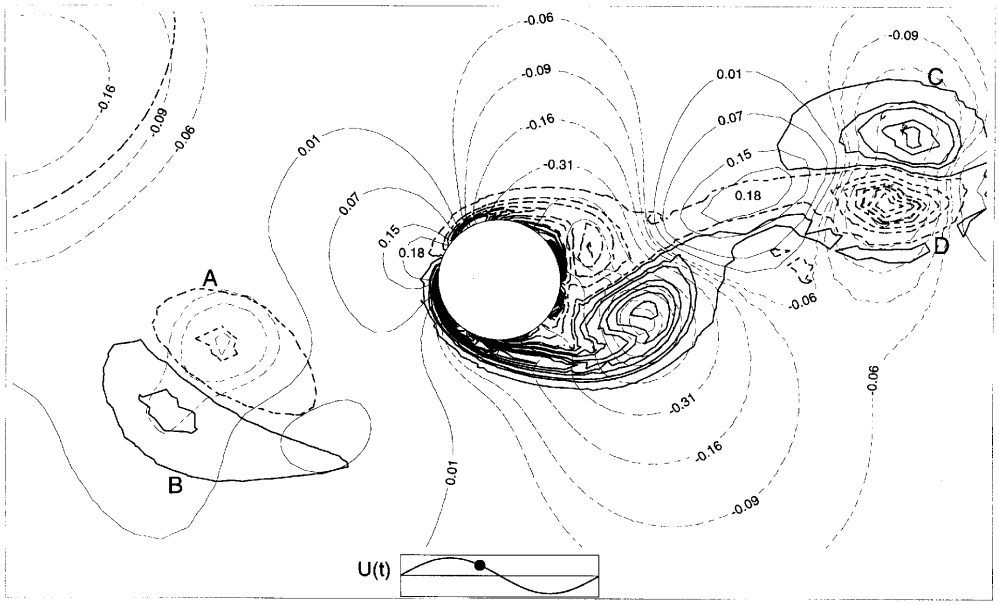

Figure 17. Pressure contours (thin lines) superimposed on equivorticity lines (thick lines) for case of Figure 16(d). The numbers represent the local values of dimensionless pressure

cycle. The results of the present study are in agreement with this rule, since for the oblique rows ($n = 1$) the lift frequency is twice the oscillation frequency, whereas for a double pair ($n = 2$) the frequency of the transverse force is three times the frequency of an oscillation cycle.

The double-pair configuration of the present solution seems to be similar to that observed for $15 < KC < 25$ at higher β. The flow pattern at corresponding phase angles agrees considerably with that derived from the experimental studies of Bearman *et al.*,[1] Williamson[2] and Obasaju *et al.*,[20] although the angle at which the vortex pair moves away from the cylinder is smaller in some cases. Another difference is that the flow pattern computed herein is periodic and the direction in which the pair convects away from the cylinder remains constant throughout all cycles. On the other hand, as reported by Bearman *et al.*[1] and Obasju *et al.*,[20] switching of the direction in which the vortices are convected can occur at different cycles, which has a critical effect on the transverse force exerted on the cylinder. A similar situation was obtained from the present solution at higher values of β, as will be explained in the following subsection.

Aperiodic shedding. Apart from the two previous well-defined vortex-shedding cases, there exists an extensive regime on the KC–β plane in which the shedding of vortices is irregular. Each pair of KC and β yields a different flow pattern which is not periodic in consecutive flow cycles. The non-periodicity of the flow pattern results in the generation of intermittent traces of the hydrodynamic forces exerted on the cylinder.

The change in the vortex-shedding pattern at different period was realized by Bearman *et al.*[1] and Obasaju *et al.*[20] For the determination of the flow mode at each cycle those researchers recorded the streamwise fluid velocity at a point on the wake centreline just behind the cylinder; the velocity signal was Fourier analysed and the various cycles were sorted according to the phase and predominant frequency. In the present numerical study the direct determination of the shedding pattern at each

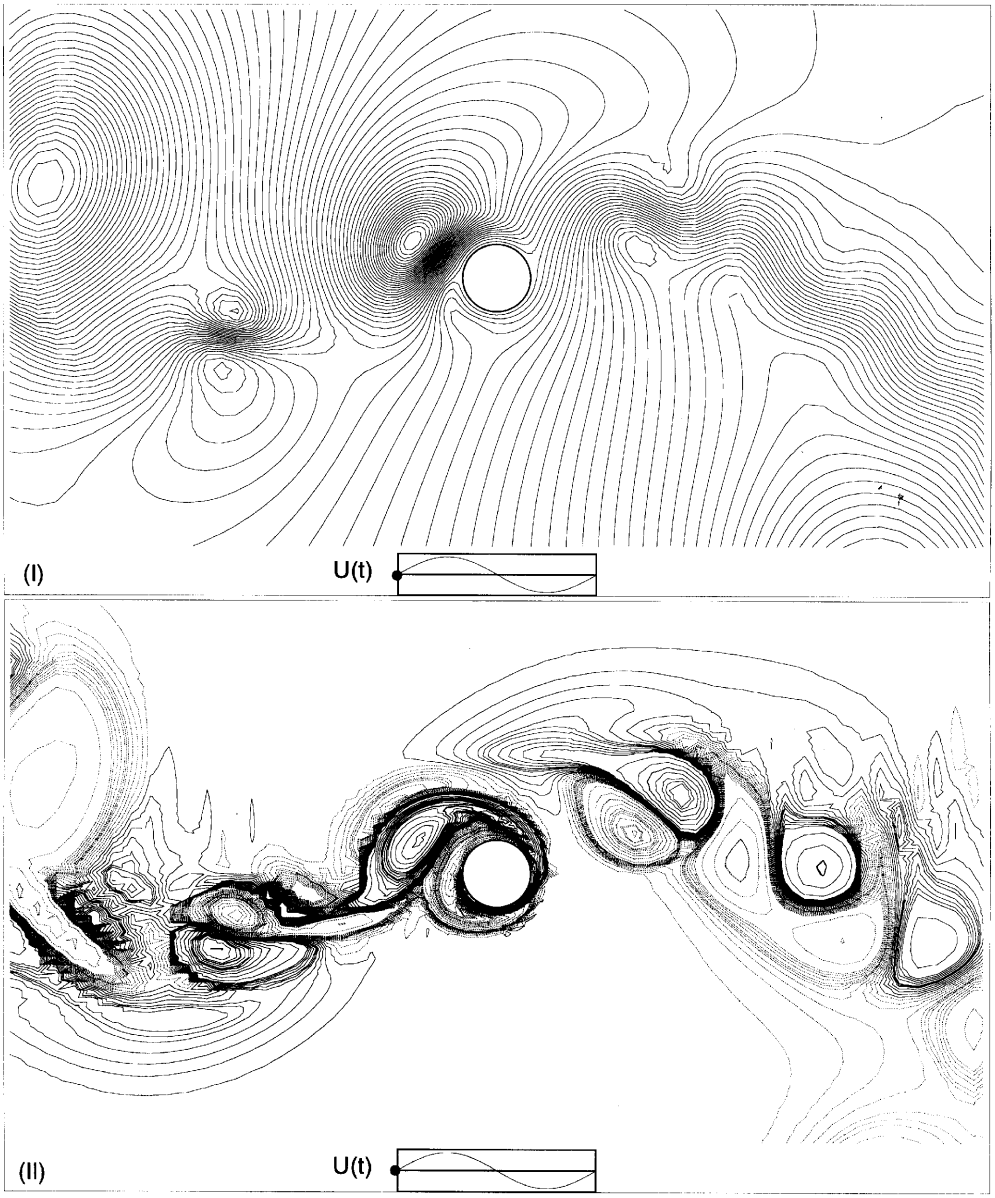

Figure 18. Enlarged view of Figure 16(a): (I) relative streamlines; (II) equivorticity lines

period was possible from the graphical representation of the flow pattern obtained from the numerical solution. It is evident that although the numerical solution gives a complete description of the flow parameters throughout the domain, which cannot be obtained experimentally, the computation over a large number of periods requires a long computer time. The CPU time required imposes limits on the number of oscillation cycles considered, which may lead to reduced reliability of the sample.

One of the flow cases studied in the aperiodic regime is that for $KC = 10$ and $\beta = 34$. The traces of the hydrodynamic forces, which are depicted in Figure 21 over a large number of cycles, display

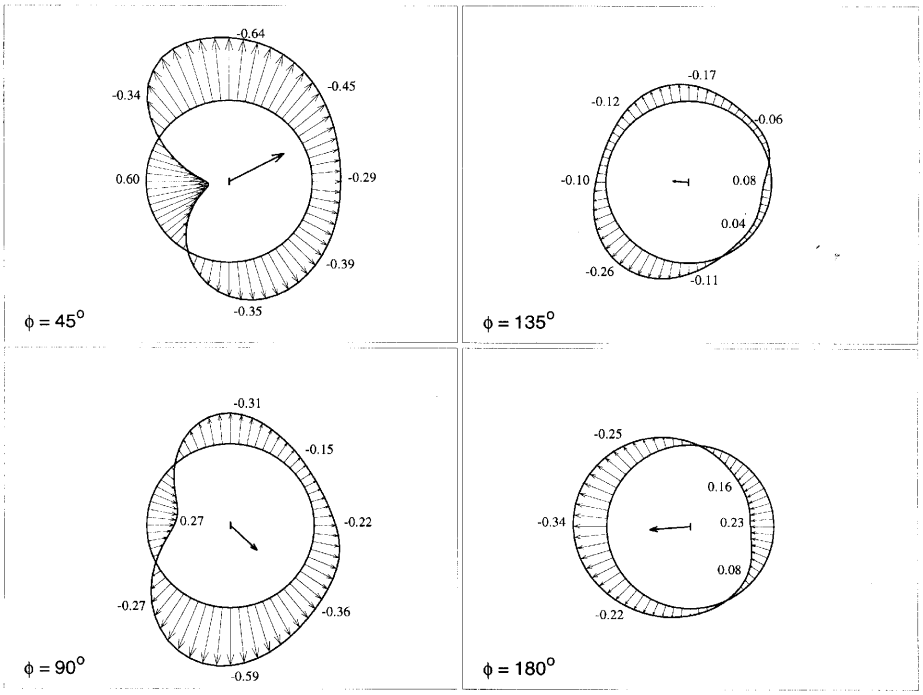

Figure 19. Pressure distribution around cylinder over one half-period for $KC = 10$ and $\beta = 20$. The numbers signify the local pressure values, while the arrow in the cylinder indicates the magnitude and direction of the resulting pressure force

fluctuations of the amplitude of the in-line and transverse forces. The time history of the hydrodynamic forces for t/T lower than 21 and higher than 24 is similar to that of Figure 20 corresponding to a double pair, whereas the decreased values of the transverse force at t/T between 21 and 24 suggest a temporal alteration of the flow pattern. An interesting feature is the opposite sign of the transverse force at the same phase angle over a period in the double-pair case before and after the transition. It is evident that at $t/T < 21$ the transverse force is positive at the beginning of each period, whereas at $t/T > 24$ it has become negative. This suggests a change in the direction in which each vortex pair is convected away from the cylinder.

The equivorticity lines at t/T between 21·5 and 24, when the stream velocity becomes equal to zero (phase angle equals 0° or 180°), are presented in Figure 22. The flow pattern varies substantially at different periods, although the phase angle is the same. In Figure 22(a) the flow pattern is similar to that of a transverse vortex street occurring at higher values of β for KC ranging between 7 and 13, observed also by Tatsuno and Bearman[4] at KC and β in the same range as in the present investigation. It is interesting to note the similarity of Figure 22(a) to Justesen's[11] solution for $KC = 8$ and $\beta = 196$. The almost symmetric flow pattern with respect to the wake centreline in Figures 22(d)–22(f) is compatible with the low values of the transverse force at t/T between 23 and 24.

The equivorticity lines over the period commencing at $t/T = 25$ are presented in Figure 23. The flow pattern is similar to the double pair depicted in Figures 15 and 16, as anticipated from the traces of the transverse force. The difference is that the pair of vortices is convected below the cylinder in the first half of the period, in agreement with the trace of the transverse force, and the flow is not absolutely periodic.

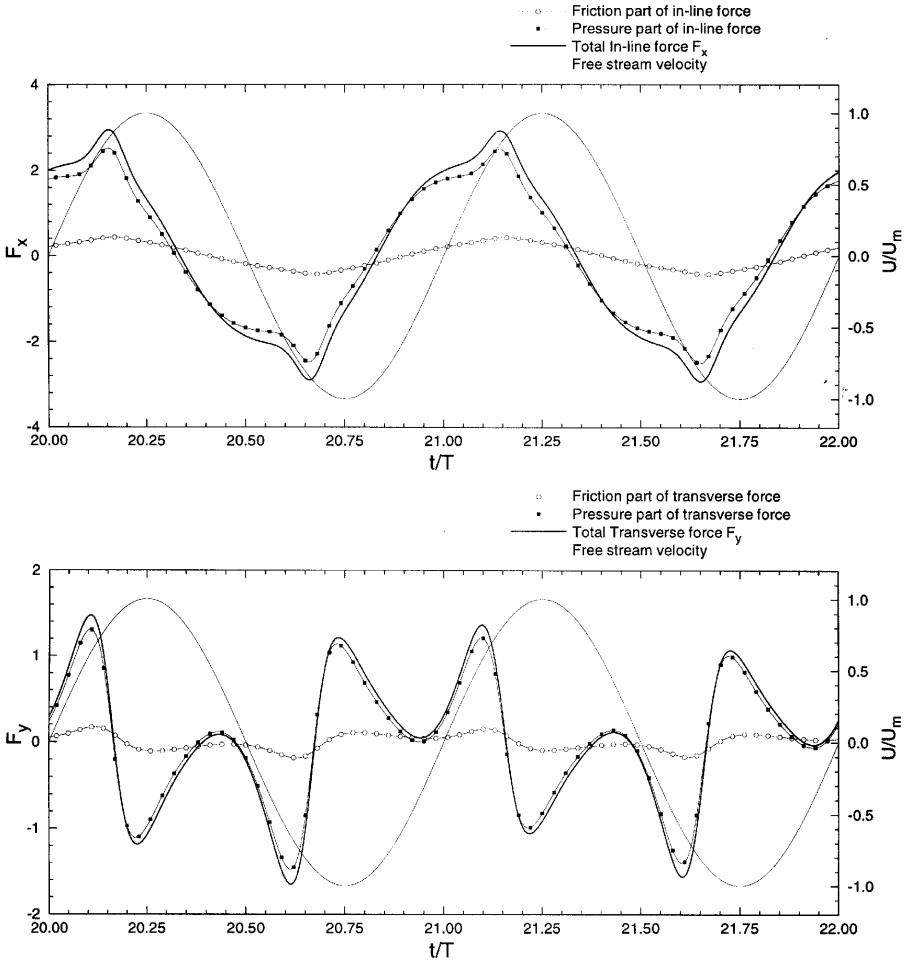

Figure 20. Traces of hydrodynamic forces during two oscillation periods for $KC = 10$ and $\beta = 20$

Another solution in the aperiodic regime was obtained for $KC = 6{\cdot}25$ and $\beta = 53$. Tatsuno and Bearman's[4] Figure 3 shows that this point lies near the boundary between the oblique vortex rows, the double pair and the aperiodic flow on the KC–β plane, therefore it is an interesting case for investigation of the transition. The time history of the hydrodynamic forces is depicted in Figure 24. The in-line force is very close to sinusoidal, with a small fluctuation of the amplitude, whereas the transverse force displays an irregular character depending on the flow mode of the cycle considered. For example, for the cycle beginning at $t/T = 51$, the trace of the lift force reveals a double pair, whereas at t/T between 52·4 and 53·4 the oblique shedding seems to be dominant. The vorticity contours confirmed that for t/T ranging between 51 and 52, the flow pattern is that of a double pair. In order to investigate the transition mechanism, the equivorticity lines for $KC = 6{\cdot}25$ and $\beta = 53$ for t/T ranging between 51·95 and 53·35 are presented in Figure 25. Comparing Figures 25(a)–25(c) with Figures 25(f)–25(h) at equal phase angles of the following period, we can easily confirm the non-periodic character of the phenomenon. The flow pattern near the cylinder in Figures 25(a) and 25(b) is almost symmetrical with respect to the wake centreline. Figure 25(c) shows a vorticity pattern whose configuration near the cylinder is similar to that of Figure 13(d), which represents the

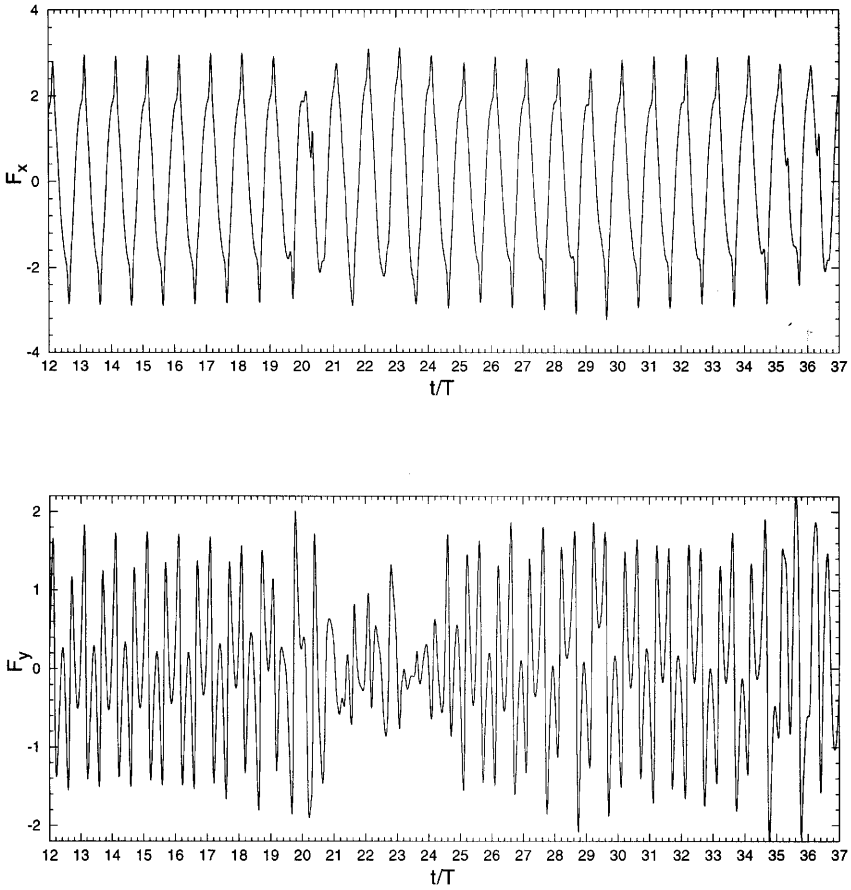

Figure 21. Traces of hydrodynamic forces during many oscillation periods for $KC = 10$ and $\beta = 34$

oblique rows case. When the phase angle has exceeded 180° in Figure 25(d), the flow pattern near the cylinder becomes similar to that of Figure 13(f). The similarity to the oblique shedding case near the cylinder is preserved throughout the sequence of frames in Figures 25(d)–25(h). The vortices convected away from the cylinder do not form rows tilted with respect to the horizontal axis, but instead seem to accumulate around the wake centreline upstream and downstream from the cylinder.

Another case of particular interest is that for $KC = 10$ and $\beta = 53$. The solution over a large number of oscillation cycles revealed that the dominant flow pattern is that of a double pair, but the direction in which the vortex pair is convected away from the cylinder does not remain constant. This change in direction can be interpreted with reference to the sequence of equivorticity lines presented in Figure 26. As the stream velocity changes direction, the vortex A of Figure 26(a) is swept downstream and pairs up with vortex B, as shown in Figure 26(b). In Figure 26(d) the counter-rotating pair A–B has moved further downstream, whereas the vortex D of Figure 26(c) has been split into two parts, denoted as D_1 and D_2. In Figure 26(e) the vortices D_1 and D_2 have been convected in the flow direction, the vortex D_2 having formed a pair with the counter-rotating vortex C. The vortex E of Figure 26(f) appears displaced far upstream from the cylinder and at a higher level compared with the corresponding vortex A of the previous cycle. As a result, the vortex E remains upstream and above the wake centreline as the flow direction reverses, as shown in Figure 26(g). In Figure 26(h) the

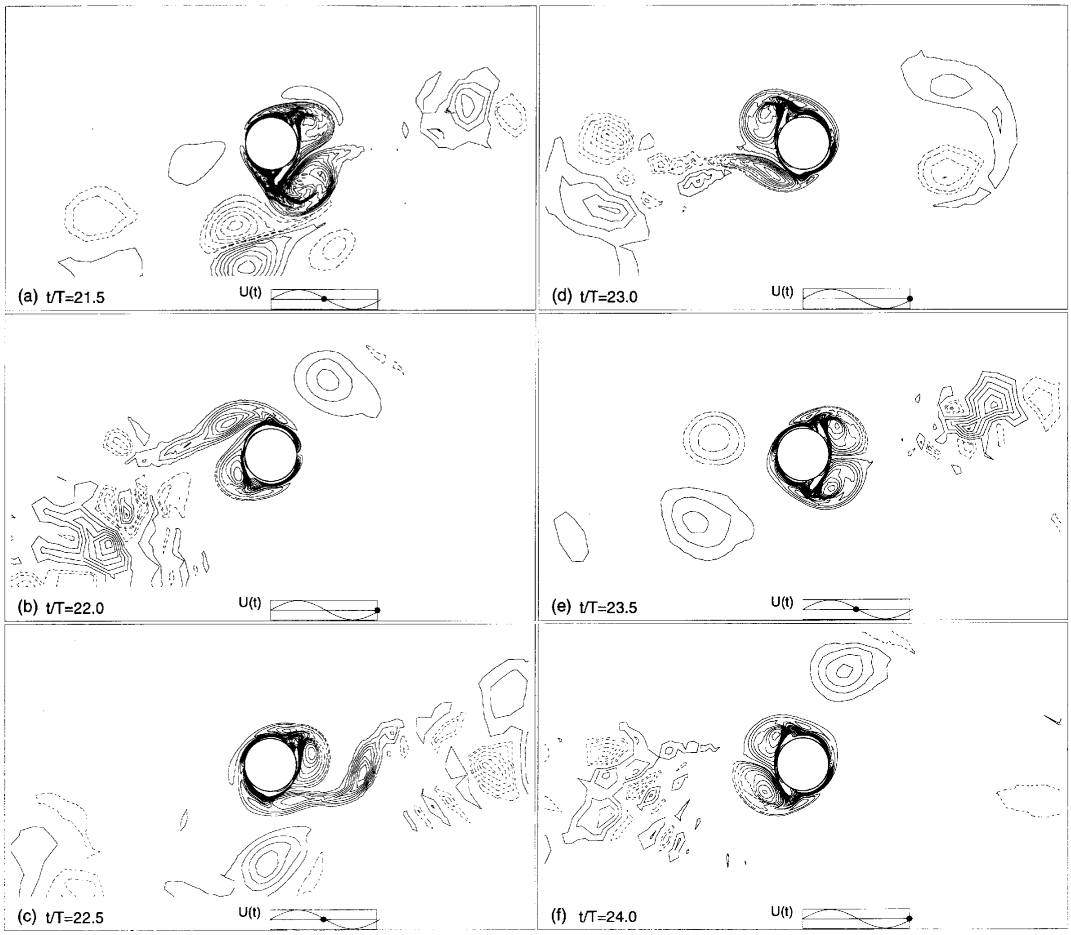

Figure 22. Vorticity contours for t/T between 21·5 and 24 when stream velocity becomes equal to zero; $KC = 10$ and $\beta = 34$

vortex E has been convected over the cylinder, whereas in Figure 26(i) it has come into close contact with the counter-rotating vortex C. In subsequent frames the vortices C and E pair up and are displaced far from the cylinder in the flow direction. After the shedding of the vortex F, the vortex G of Figure 26(k) has been formed at the opposite side of the cylinder from the vortex A of Figure 26(a), therefore the vortex pair G–H of Figure 26(l) moves away from the cylinder in the opposite direction from the pair A–B of Figure 26(b) at the same phase angle but two oscillation cycles earlier. It should be remembered that this switching has been found experimentally by Bearman *et al.*[1] and Obasaju *et al.*[20] at *KC* between 15 to 25 for higher values of the frequency parameter.

For a better interpretation of the various shedding modes the equivorticity lines over 12 successive cycles are displayed in Figure 27 for $\phi = 68°$. In Figures 27(a), 27(d), 27(f) and 27(h) the flow pattern is that of a double pair. In most cases the vortex pair is convected below the cylinder during the first half of the oscillation cycle, whereas only in Figure 27(f) does the vortex pair move away from the cylinder above the centreline of the wake. In Figures 27(e) and 27(j) we can see the negative sign vortices in contact with the leading edge of the cylinder. As explained previously, these vortices failed to cross over the cylinder as the flow direction changed, remaining upstream from the cylinder. The effect of this 'failure' is the intermission of the double-pair sequence.

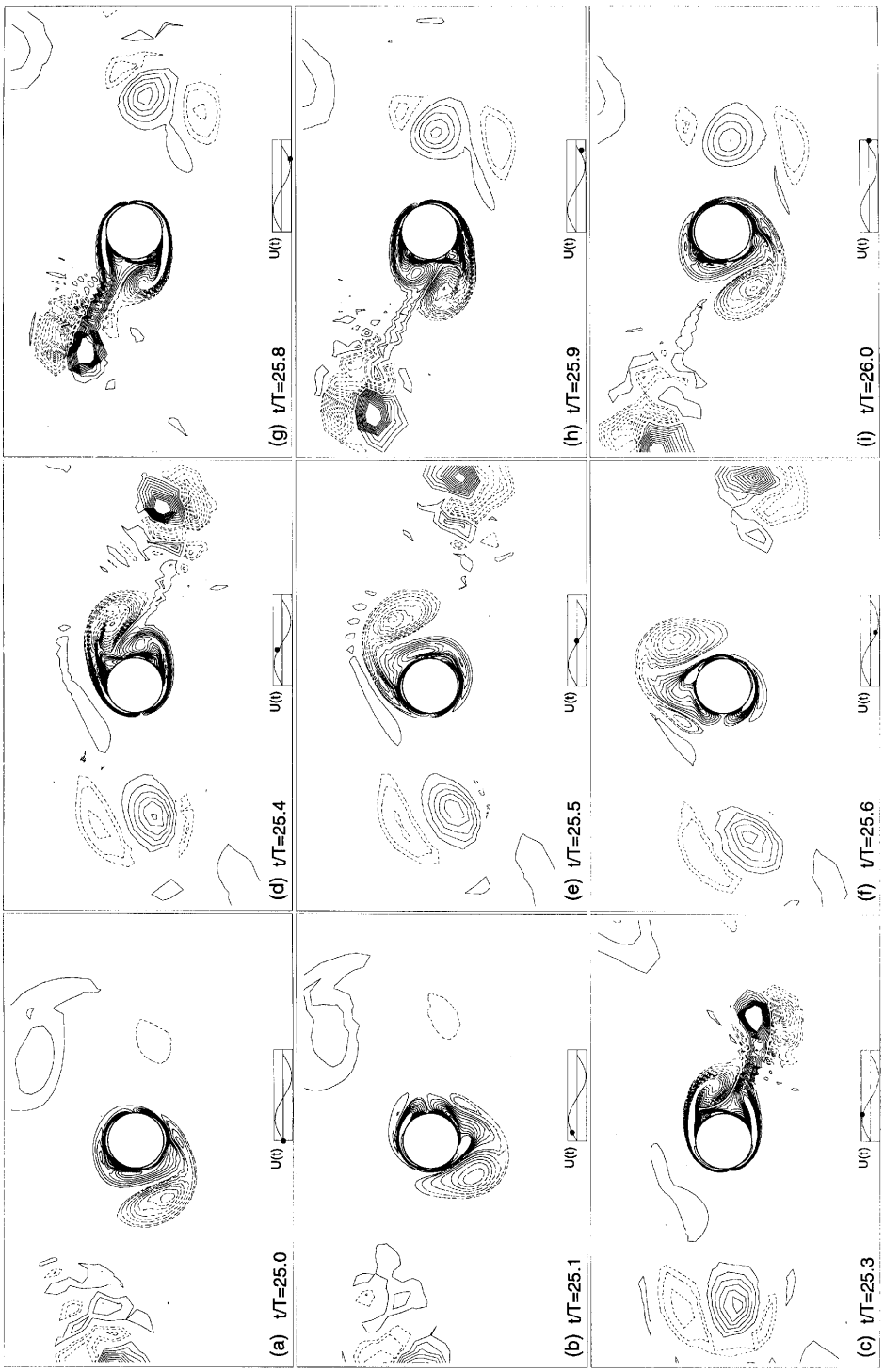

Figure 23. Vorticity contours for cycle beginning at $t/T = 25$; $KC = 10$ and $\beta = 34$

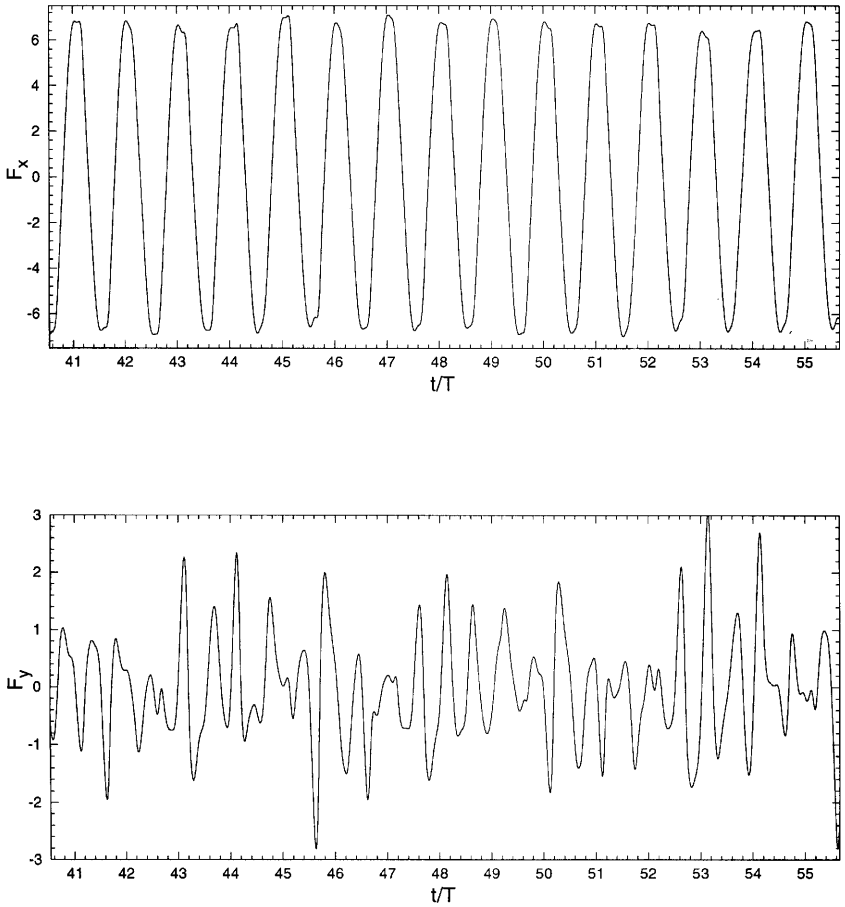

Figure 24. Traces of hydrodynamic forces during many oscillation periods for $KC = 6{\cdot}25$ and $\beta = 53$

The time history of the hydrodynamic forces over 14 oscillation cycles, including those of Figure 27, is depicted in Figure 28. In some intervals the force traces corresponding to a double pair are recognizable, while in others they display an irregular character. The transverse force is more susceptible to the alteration of the flow pattern than the in-line force. The traces of the hydrodynamic forces for t/T between 24 and 29 are shown in Figure 29 on a different time scale. At the first and last periods shown, the transverse force is that of a double pair, convecting below the cylinder in the first half of the period. On the other hand, for the cycle beginning at $t/T = 26$, the trace of the transverse force is that of a double pair moving away from the cylinder in the opposite direction, whereas when t/T lies between 27 and 28, the transverse force displays a random character. The force traces of each cycle are compatible with the flow pattern of Figure 27.

The three previous examples provide a good idea of the complexity of the flow pattern in the aperiodic regime, a prominent characteristic of which is the switching of modes at different cycles. For points on the KC–β plane close to the boundary with the periodic flow, the prevalent flow modes are those of the periodic patterns closest to the point considered. An interesting feature of this regime is the appearance of the transverse street, a flow pattern not observed in the periodic regime for this KC and β range.

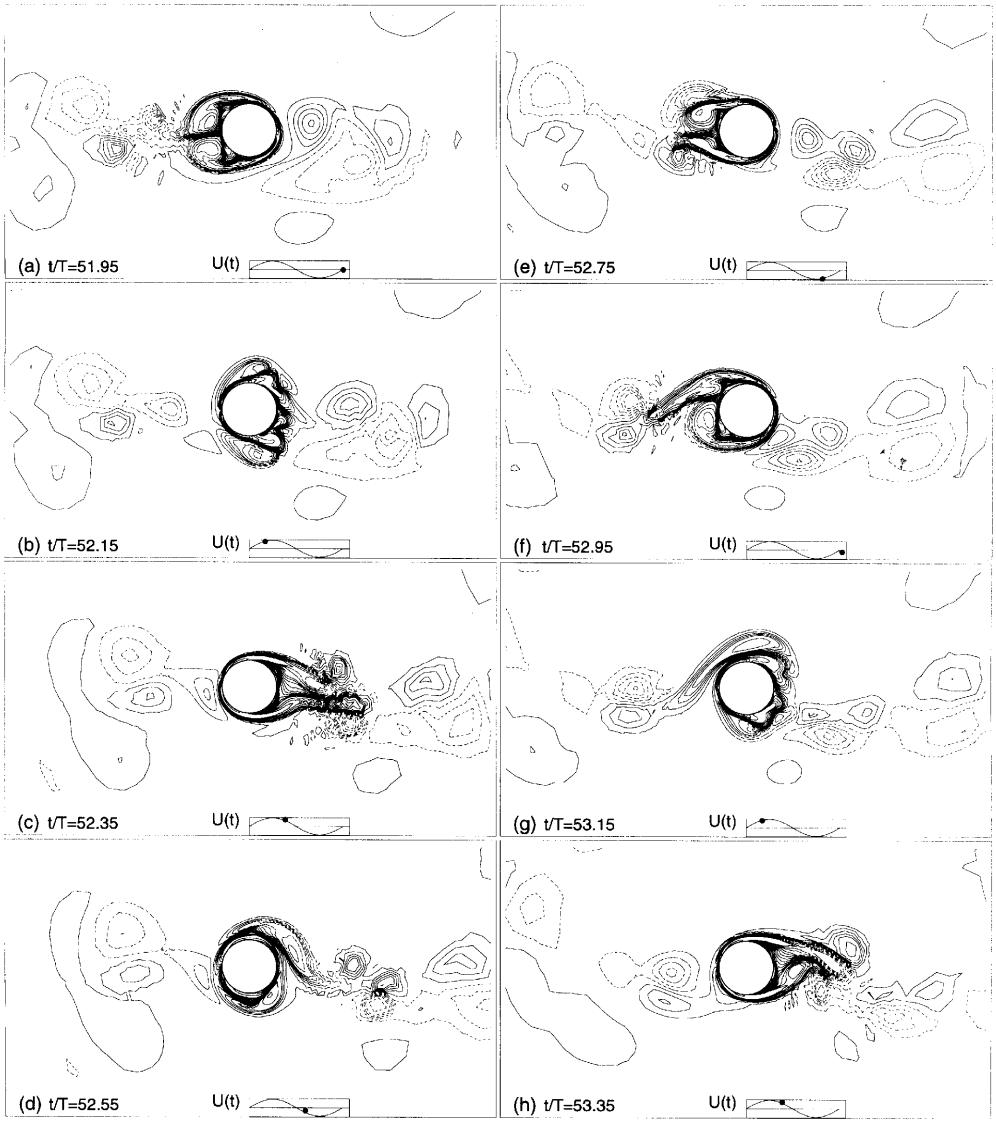

Figure 25. Vorticity contours for t/T between 51·95 and 53·35; $KC = 6{\cdot}25$ and $\beta = 53$

3.3. *Hydrodynamic coefficients of in-line force*

Morison *et al.*[22] proposed that the total in-line force exerted per unit length of a cylinder in an oscillating flow can be expressed as the sum of two components,

$$F_x^* = \tfrac{1}{2}\rho D C_D U|U| + \tfrac{1}{4}\pi\rho D^2 C_M \dot{U}, \tag{28}$$

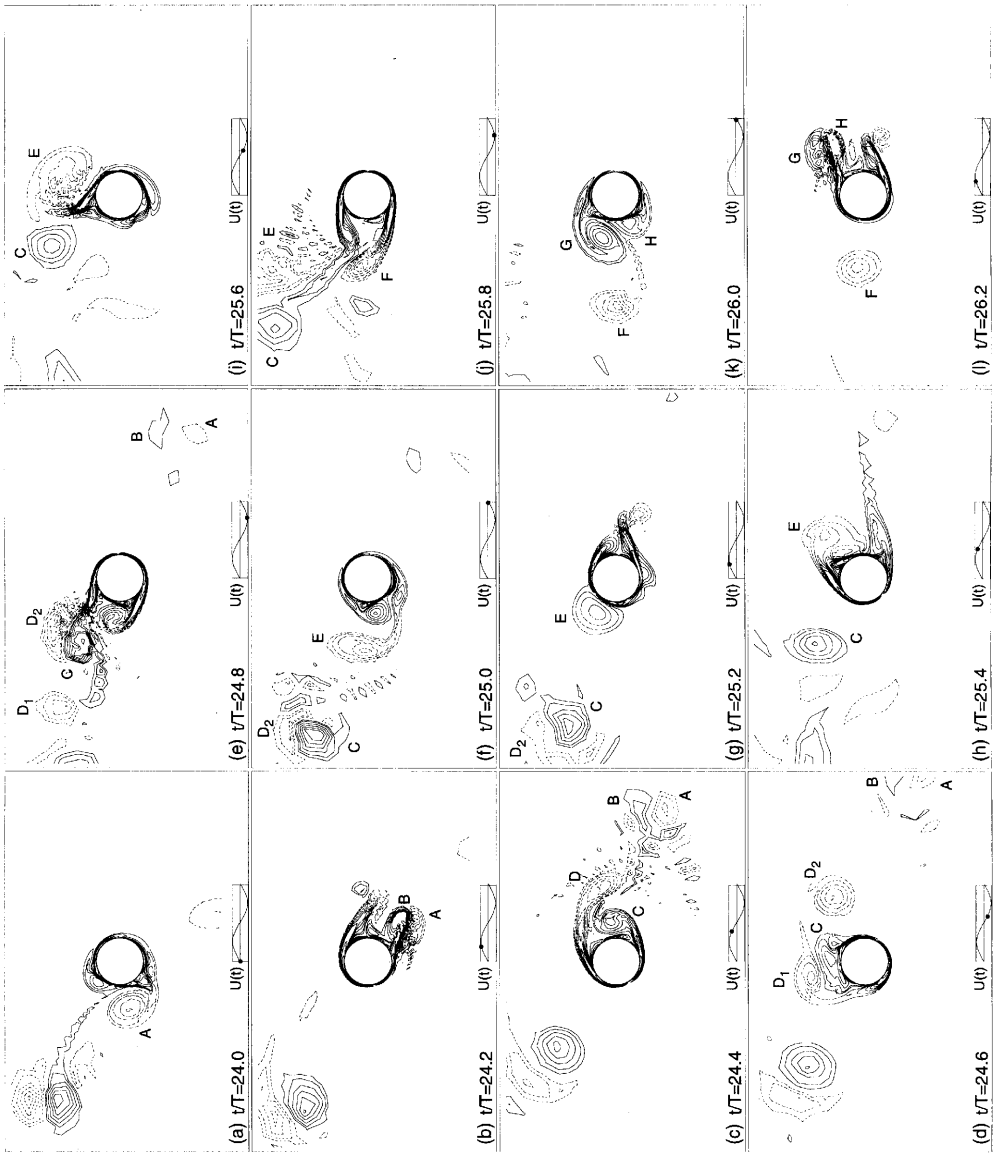

Figure 26. Vorticity contours over two consecutive oscillation cycles starting at $t/T = 24$; $KC = 10$ and $\beta = 53$

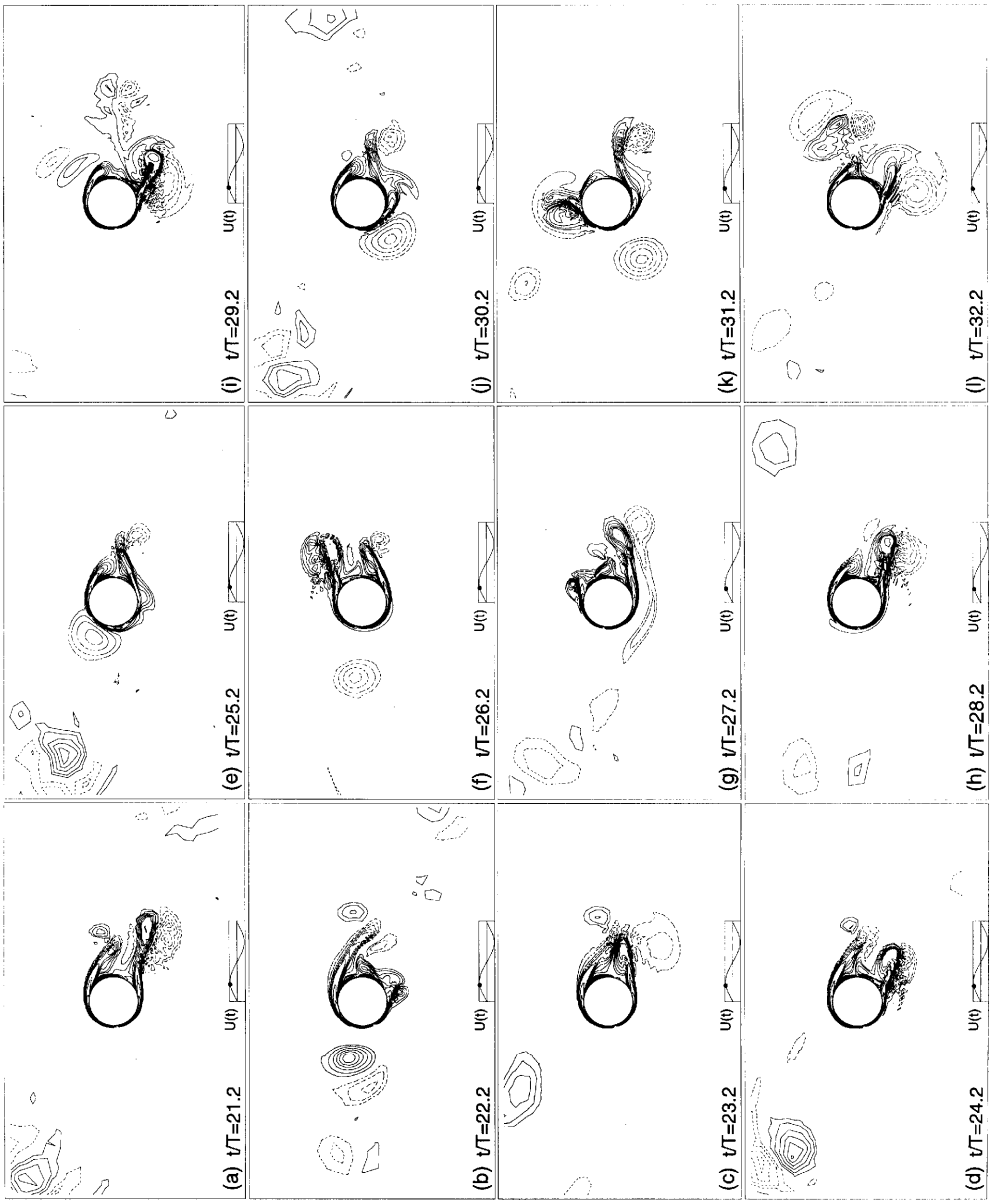

Figure 27. Vorticity contours at 12 consecutive cycles when phase angle is 68°; $KC = 10$ and $\beta = 53$

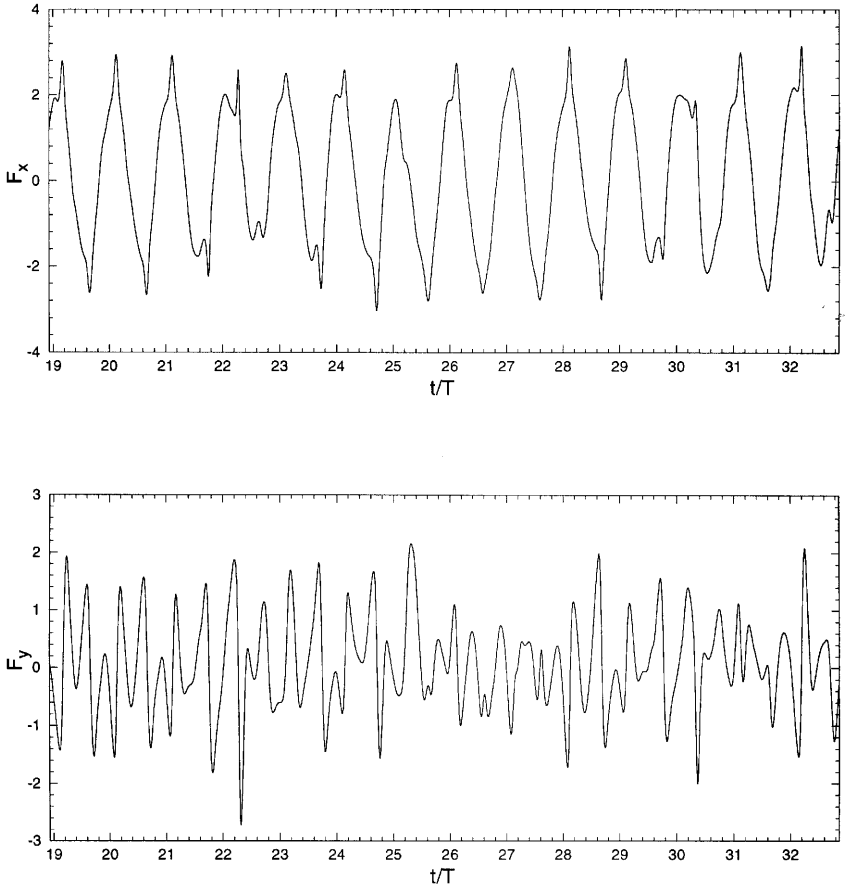

Figure 28. Traces of hydrodynamic forces during many oscillation periods for $KC = 10$ and $\beta = 53$

where ρ is the fluid density and C_D and C_M are the drag and inertia coefficients. The Fourier-averaged coefficients C_D and C_M for a cylinder immersed in an oscillating flow, as defined by (8), are given by[23]

$$C_D = \frac{3}{8}\int_0^{2\pi} \frac{F_x^* \sin\phi}{0{\cdot}5\rho U_m^2 D}\, d\phi, \tag{29}$$

$$C_M = \frac{U_m T}{\pi^3 D}\int_0^{2\pi} \frac{F_x^* \cos\phi}{0{\cdot}5\rho U_m^2 D}\, d\phi, \tag{30}$$

where ϕ is the phase angle in (8).

The RMS value of the total in-line force in dimensionless form is defined as

$$F_x(\text{rms}) = \left[\frac{1}{T}\int_0^T \left(\frac{F_x^*}{0{\cdot}5\rho U_m^2 D}\right)^2 dt\right]^{1/2}. \tag{31}$$

The drag and inertial coefficients as functions of KC for $\beta = 34$ and 53 are depicted in Figures 30 and 31. Experimental results were provided at these β-values by Kuhtz,[24] who conducted force

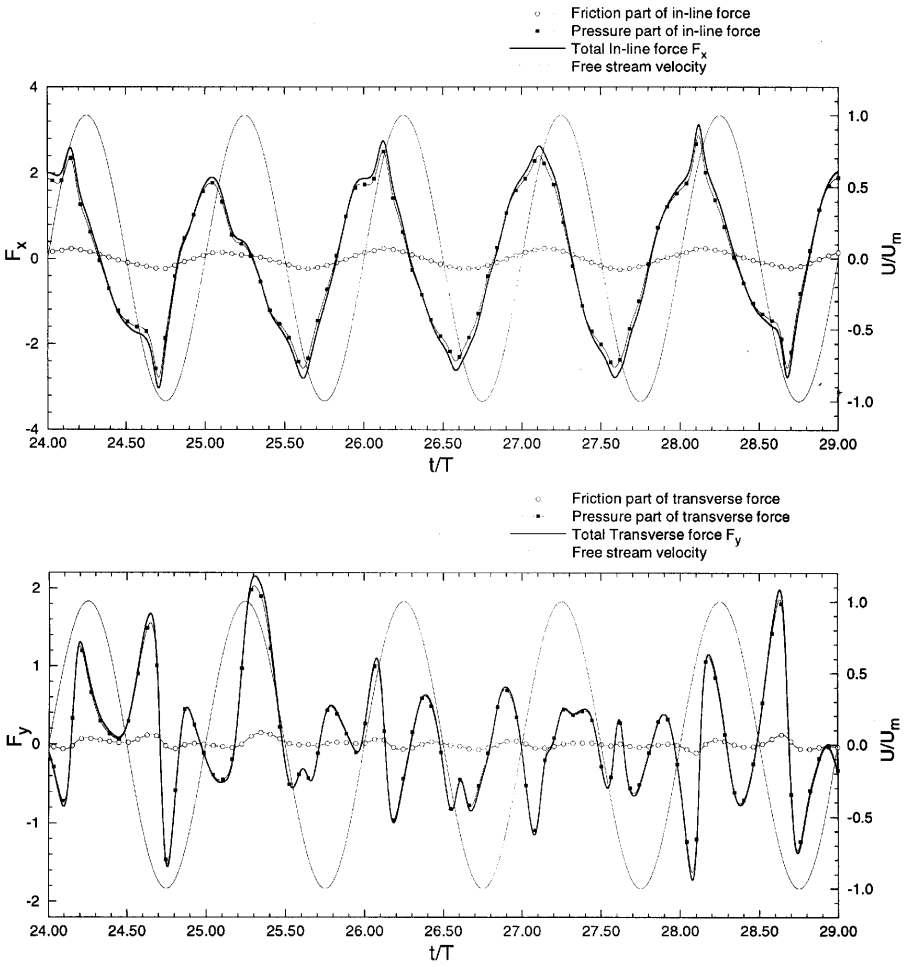

Figure 29. Traces of hydrodynamic forces for t/T between 24 and 29; $KC = 10$ and $\beta = 53$

measurements on a cylinder mounted horizontally in a U-tube; therefore the computation was conducted at the same values of β for the sake of comparison. Figures 30 and 31 reveal good agreement of the computed C_D with Wang's[7] analytical results for $KC \leqslant 1$. As KC is increased, the numerical C_D-values become slightly higher than those predicted by Wang's analysis, most likely owing to flow separation effects. It is interesting to note the agreement of the computed C_D-values with those measured by Kuhtz[24] at $KC < 8$ and the discrepancy for $KC > 8$ when $\beta = 53$.

The computed C_M-values in the lower-KC regime ($KC < 1$) are slightly higher than those predicted by Wang's analysis in both diagrams, while for KC ranging between 1 and 2, the computed C_M-values became closer to the analytical ones. For $KC > 2$ the computed C_M-values depart from those predicted by Wang. In the KC range between 2 and 8, small discrepancies are observed between the C_M-values computed by the present code and the experimental ones, which increase drastically as KC becomes greater than 8 at $\beta = 53$.

Figure 4 dictates that the discrepancy between computed and measured force coefficients is initiated when the flow becomes asymmetric, and is amplified in the aperiodic regime. For $\beta = 53$,

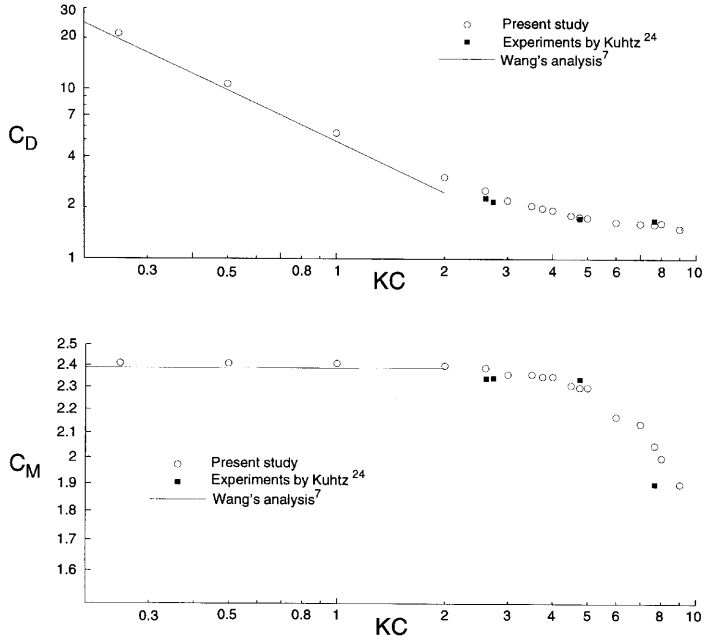

Figure 30. Hydrodynamic coefficients of in-line force as functions of KC for $\beta = 34$

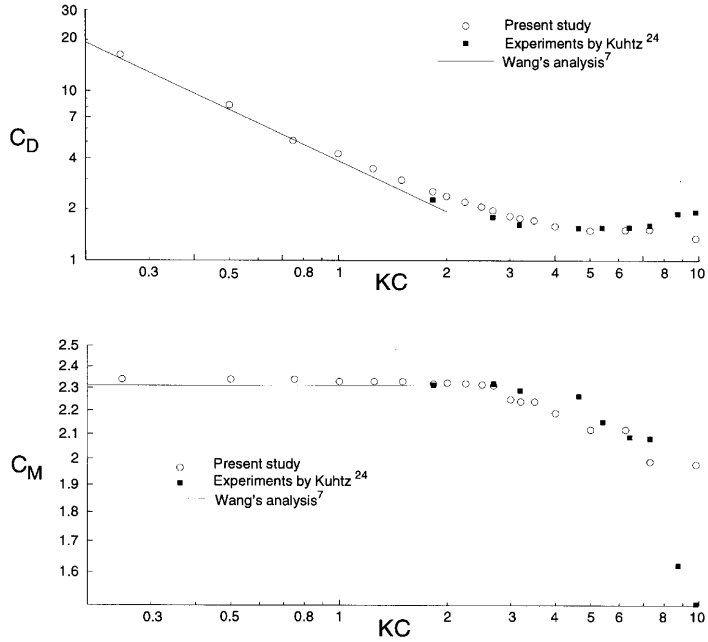

Figure 31. Hydrodynamic coefficients of in-line force as functions of KC for $\beta = 53$

when $KC > 8$, the computed C_D-values are lower than the measured ones, whereas the opposite occurs for the computed and measured values of C_M. The flow for $\beta = 53$ and $KC > 8$ is strongly aperiodic, which causes an intermittent trace of the in-line force, an example being that portrayed in Figure 28. Apparently, the non-periodicity of the force trace reflects on the Fourier-averaged values of the drag and inertia coefficients. It should be noted that the three-dimensional character of the flow occurring in the experiment, as quoted by Tatsuno and Bearman,[4] seems to have rather small influence on the magnitude of the in-line force coefficients.

The RMS value of the dimensionless in-line force calculated from (31) is presented in Figure 32 for $\beta = 34$ and in Figure 33 for $\beta = 53$. The values of F_x (rms) computed herein are higher than the predictions of inviscid theory, according to which $F_x(\text{rms}) = \sqrt{2}\,\pi^2/KC$ for small KC-values. The discrepancy can be explained by bearing in mind that in inviscid theory the contribution of shear stress is neglected, which leads to a reduced value of the in-line force.

Figures 32 and 33 show very good agreement between computed and measured values of F_x(rms), even in the cases where discrepancies in the force coefficients were detected. An interesting result is that the RMS values of the dimensionless in-line force decrease with increasing KC and are almost independent of the β. This is further substantiated by Bearman *et al.*,[21] who presented the RMS values of the non-dimensional in-line force for KC up to 10 for higher β-values.

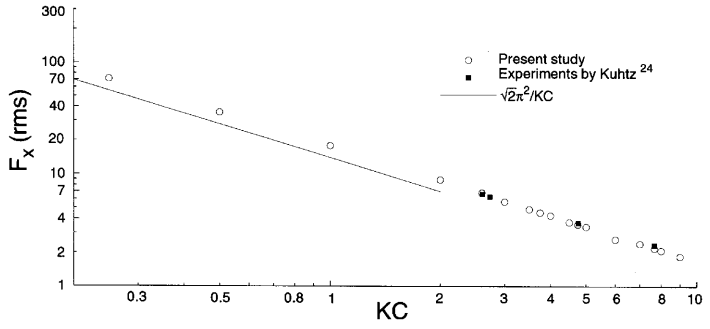

Figure 32. Root mean square value of dimensionless in-line force as a function of KC for $\beta = 34$

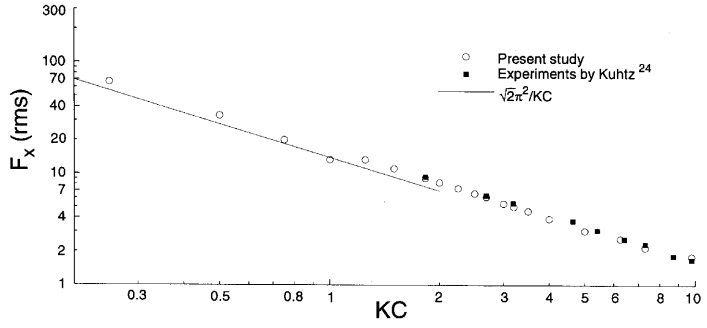

Figure 33. Root mean square value of dimensionless in-line force as a function of KC for $\beta = 53$

5. CONCLUSIONS

The finite element method was applied for the solution of two-dimensional flow around a circular cylinder in oscillating flow at low Keulegan–Carpenter numbers and frequency parameters. The computational results are in good agreement with experimental evidence under similar conditions,[4,24] which confirms the accuracy of the solution.

For low values of the Keulegan–Carpenter number the flow remains symmetrical; above a certain value of the Keulegan–Carpenter number which depends on the frequency parameter, asymmetry appears in the flow which is eventually amplified and leads to complicated vortex-shedding patterns, some of which are different from those observed at higher frequency parameters. There also exists a flow regime in which the flow is aperiodic; the solution over a large number of oscillation cycles for an extended range of KC–β pairs revealed switching of the flow between different modes.

For very low values of the Keulegan–Carpenter number the computed in-line force agrees closely with Wang's[7] asymptotic solution. When the flow remains symmetrical, the trace of the total in-line force is very close to a sine wave, while when the flow becomes asymmetric, the shedding of vortices causes the generation of higher harmonics. In the vortex-shedding regime the asymmetry of flow leads to the development of a transverse force, whose time history depends on the vortex-shedding mode. The non-periodic character of flow in the aperiodic regime reflects on the traces of the hydrodynamic forces.

The flow visualization study by Tatsuno and Bearman[4] revealed that in the largest part of the KC–β plane the flow is three-dimensional. The resolution of flow in three dimensions is beyond the capability of the present two-dimensional computer code. The agreement between the results of the present solution and experiments suggests that the three-dimensional character of the flow has a minor effect on the principal feature of the flow pattern and on the magnitude of the in-line force exerted on the cylinder.

ACKNOWLEDGEMENTS

The present project was supported financially by the Science Programme of the European Community, Contract SCI*-CT92-0812. G.I. also received a research grant from the Greek Foundation of National Awards (IKY).

REFERENCES

1. P. W. Bearman, J. M. R. Graham, P. Naylor and E. D. Obasaju, 'The role of vortices in oscillatory flow about bluff bodies', *Proc. Int. Symp. on Hydrodynamics in Ocean Engineering*, Trondheim, 1981, pp. 621–635.
2. C. H. K. Williamson, 'Sinusoidal flow relative to circular cylinders', *J. Fluid Mech.*, **155**, 141–174 (1985).
3. T. Sarpkaya, 'Forces on a circular cylinder in viscous oscillatory flow at low Keulegan–Carpenter numbers', *J. Fluid Mech.*, **165**, 61–71 (1986).
4. M. Tatsuno and P. W. Bearman, 'A visual study of the flow around an oscillating cylinder at low Keulegan–Carpenter number and low Stokes numbers', *J. Fluid Mech.*, **211**, 157–182 (1990).
5. H. Honji, 'Streaked flow around an oscillating circular cylinder', *J. Fluid Mech.*, **107**, 509–520 (1981).
6. G. G. Stokes, 'On the effect of the internal friction of fluids on the motion of pendulums', *Trans. Camb. Philos. Soc.*, **9**, 8–106 (1851).
7. C.-Y. Wang, 'On the high frequency oscillating viscous flows', *J. Fluid Mech.*, **32**, 55–68 (1968).
8. N. Baba and H. Miyata, 'Higher-order accurate difference solutions of vortex generation from a circular cylinder in an oscillatory flow', *J. Comput. Phys.*, **69**, 362–396 (1987).
9. S. Murashige, M. Hinatsu and T. Kinoshita, 'Direct calculations of the Navier–Stokes equations for forces acting on a cylinder in oscillatory flow', *Proc. Eighth Int. Conf. on Offshore Mechanics and Arctic Engineering*, The Hague, 1989, Vol. 2, pp. 411–418.
10. X. Wang and C. Dalton, 'Oscillating flow past a rigid circular cylinder: a finite difference calculation', *ASME J. Fluids Engng.*, **113**, 377–383 (1991).
11. P. Justesen, 'A numerical study of oscillating flow around a circular cylinder', *J. Fluid Mech.*, **222**, 157–196 (1991).

12. N. G. Skomedal, T. Vada and B. Sortland, 'Viscous forces on one and two circular cylinders in planar oscillatory flow', *Appl. Ocean Res.*, **11**, 114–134 (1989).
13. J. M. R. Graham and B. Djahansouzi, 'Hydrodynamic damping of structural elements', *Proc. Eighth Int. Conf. on Offshore Mechanics and Arctic Engineering*, The Hague, 1989, Vol. 2, pp. 289–293.
14. P. A. Smith and P. K. Stansby, 'Viscous oscillatory flows around cylindrical bodies at low Keulegan–Carpenter numbers using the vortex method', *J. Fluids Struct.*, **5**, 339–361 (1991).
15. P. Anagnostopoulos, G. Iliadis and J. Rasoul, 'Numerical solution of oscillatory flow around a circular cylinder at low Reynolds and Keulegan–Carpenter numbers', *Proc. Eighth Int. Conf. on Finite Elements in Fluids*, Barcelona, 1993, pp. 258–267.
16. S. L. Smith and C. A. Brebbia, 'Finite element solution of Navier–Stokes equations for transient two-dimensional incompressible flow', *J. Comput. Phys.*, **17**, 235–245 (1975).
17. S. L. Smith and C. A. Brebbia, 'Improved stability techniques for the solution of Navier–Stokes equations', *Appl. Math. Model.*, **1**, 226–234 (1977).
18. P. Anagnostopoulos, 'Numerical solution for laminar two-dimensional flow about a fixed and transversely oscillating cylinder in a uniform stream', *J. Comput. Phys.*, **85**, 434–456 (1989).
19. P. Anagnostopoulos, 'Computer-aided flow visualization and vorticity balance on the laminar wake of a circular cylinder', *J. Fluids Struct.*, **11**, 33–72 (1997).
20. E. D. Obasaju, P. W. Bearman and J. M. R. Graham, 'A study on forces, circulation and vortex patterns around a circular cylinder in oscillatory flow', *J. Fluid Mech.*, **196**, 467–494 (1988).
21. P. W. Bearman, M. J., Downie, J. M. R. Graham and E. D. Obasaju, 'Forces on cylinders in viscous oscillatory flow at low Keulegan–Carpenter numbers', *J. Fluid Mech.*, **154**, 337–356 (1985).
22. J. R. Morison, M. P. O'Brien, J. W. Johnson and S. A. Schaff, 'The force exerted by surface waves on piles', *Petrol. Trans.*, **189**, 149–157 (1950).
23. T. Sarpkaya, 'Vortex shedding and resistance in harmonic flow about smooth and rough circular cylinders at high Reynolds numbers', *Tech. Rep. NPS-59SL76021*, Naval Postgraduate School, Monterey, CA, 1976.
24. S. Kuhtz, 'Experimental investigation of oscillatory flow around circular cylinders at low beta numbers', *Ph.D. Thesis*, University of London, 1996.

